Petroleum Science 23 (2026) 1233–1249

Contents lists available at ScienceDirect

Petroleum Science

journal homepage: www.keaipublishing.com/en/journals/petroleum-science

Original Paper

Dynamic deconvolution based on adaptive local frequency modulation transform

Mi-Mi Huang, Zhao-Yun Zong *, Xiao-Jun Lian, Yi Shen, Ji-Dong Yang, Qing-Feng Meng

State Key Laboratory of Deep Oil and Gas, China University of Petroleum (East China), Qingdao, 266580, Shandong, China

ARTICLE INFO

Article history:
Received 7 August 2025
Received in revised form
29 October 2025
Accepted 28 November 2025
Available online 3 December 2025

Edited by Meng-Jiao Zhou

Keywords:
Absorption attenuation
High resolution
Dynamic deconvolution
Time-frequency analysis method

ABSTRACT

Dynamic deconvolution in the time-frequency domain is an effective method to improve seismic resolution. However, the traditional methods usually suffer from the limitation of window width and shape, resulting in insufficient time-frequency resolution and phase distortion of seismic signatures, which significantly limits their applicability in complex geological conditions. To overcome this problem, we propose an adaptive local frequency modulation transform (ALFMT), which is directly embedded in the dynamic deconvolution method. ALFMT can dynamically adjust the shape of the analysis window based on the adaptive local frequency information so that the time-frequency energy is effectively focused near the local frequency, thereby improving the focusing and resolution of the time-frequency representation. The synthetic examples and actual seismic application demonstrate that the ALFMT-based dynamic deconvolution can effectively compensate for the seismic amplitude energy, and the compensated data has a higher resolution and clearer reflection characteristics.

1. Introduction

High signal-to-noise ratio and high-resolution seismic data play an important role in geo-energy exploration and geological disaster forecasting (Xie et al., 2024; Zhang et al., 2024). However, many factors such as, source excitation characteristics, strata absorption attenuation, and the attributes of receiving instruments, usually lead to the significant reduction of seismic amplitude and dominant frequency as well as the phase distortion, which in turn causes a decrease of the resolution of acquired seismic data (Chen et al., 2022, 2024; Ma et al., 2022). To compensate for the seismic attenuation and improve the seismic data quality, a large amount of seismic high-resolution processing methods, such as inverse *Q*-filtering (Hargreaves and Calvert, 1991; Tu and Lu, 2009; Chen et al., 2023), spectral whitening (Manenti et al., 2018; Wang et al., 2025), and deconvolution (Gibson and Larner, 1984; Wang, 2022) are developed sequentially. Despite their demonstrated effectiveness in improving seismic resolution in practical scenarios, these methods are constrained by intrinsic limitations. For example, accurately estimating formation *Q* values remains a significant challenge in inverse *Q* filtering (Wang, 2006, 2004; Zhou and Rao, 2018). Maintaining stability in amplitude recovery remains challenging for spectral whitening (Naghadeh and Morley, 2017). Conventional deconvolution fails to account for the attenuation characteristics of the source wavelet during propagation (Chen et al., 2013; Zhou et al., 2014; Du et al., 2021).

To account for amplitude attenuation and phase distortion due to the viscoelastic and heterogeneous properties of the subsurface, Margrave et al. developed and refined the Gabor deconvolution method under the assumptions of minimum-phase wavelets and white noise reflectivity (Margrave, 1998; Margrave et al., 2002, 2011). This method does not require deterministic *Q*-value estimation and has been successfully applied in practical seismic data processing. Nevertheless, the time-frequency characteristics of seismic signals vary during propagation in complex subsurface media, indicating their nonstationary nature. However, the fixed window size in the Gabor transform results in limited time-frequency resolution. In addition, it fails to address the errors caused by phase distortion in nonstationary seismic records during the transformation from the time-frequency domain back to the time domain. Therefore, high-resolution time-frequency analysis remains essential for obtaining detailed spectra of nonstationary seismic signals.

With the growing demand for characterizing the nonstationary features of seismic data in signal processing and interpretation, a

* Corresponding author.
E-mail address: zongzhaoyun@upc.edu.cn (Z.-Y. Zong).
Peer review under the responsibility of China University of Petroleum (Beijing).

https://doi.org/10.1016/j.petsci.2025.11.048

series of time-frequency analysis methods have emerged. These include linear approaches such as the Gabor transform (Gabor, 1946; Li and Liu, 2018), short-time Fourier transform (STFT) (Auger et al., 2012), continuous wavelet transform (CWT) (Mallat, 1989; Wang et al., 2017; Tian et al., 2022a, 2022b), S-transform (ST) (Pinnegar and Mansinha, 2003; Lin, 2011; Wang et al., 2021), W-transform (WT) (Wang, 2021; Luo and Zong, 2023; Wang et al., 2024), bilinear time-frequency analysis methods such as Wigner-Ville distribution (WVD) (Cohen, 1989), and adaptive decomposition time-frequency analysis methods such as matching pursuit (Zhang et al., 2016; Zong et al., 2023; Li, 2024) and Hilbert-Huang transform (Huang and Wu, 2008). These developments have strongly advanced time-frequency analysis for nonstationary signals. Among them, the STFT performs local Fourier transforms on the signal using a fixed window. Although computationally simple, it struggles to balance time and frequency resolution. The CWT constructs scale-based dynamic windows using a mother wavelet, enabling multiscale and multiresolution analysis. However, its frequency representation is not sufficiently intuitive, and it lacks explicit phase information. On this basis, the ST incorporates frequency-dependent windowing, combining the frequency localization capability of the STFT with the multi-scale characteristics of the CWT. Furthermore, the W-transform builds upon the S-transform by introducing a smoothed instantaneous frequency to modulate the window shape, effectively enhancing time resolution at low frequencies.

However, the smoothed instantaneous frequency often suffers from poor stability. It is also sensitive to boundary effects, which may introduce non-physical values. These issues can lead to incorrect compression or stretching of the window function. In contrast, local frequency exhibits stronger noise resistance and can more accurately characterize the attenuation features of seismic waves. It is more sensitive to weak, attenuated signals, avoids the zero-division problem, and offers a clearer physical interpretation. Therefore, we propose an adaptive local frequency modulated transform (ALFMT), which enhances time-frequency concentration and improves the detection of weak signals by introducing a window shape adaptively modulated by local frequency. On this basis, we further proposed a dynamic deconvolution method based on ALFMT. This method integrates the high-resolution capability of time–frequency analysis into a nonstationary convolution model to better characterize time-varying seismic signals. Finally, we demonstrate the validity and effectiveness of the proposed method through numerical simulations and the processing of field data.

2. Adaptive local frequency modulation transform

For any signal $x(t)$, the continuous form of its short-time Fourier transform can be expressed as:

$$\mathrm{STFT}(\tau,f)=\int_{-\infty}^{\infty}x(t)h(\tau-t)\mathrm{e}^{-i2\pi ft}\mathrm{d}t, \tag{1}$$

where $i=\sqrt{-1}$ is the imaginary unit; τ is the time shift factor; t and f represent time and frequency, respectively; the window function $h(t)$ is as follows:

$$h(t)=\frac{1}{\sigma\sqrt{2\pi}}\mathrm{e}^{-\frac{t^2}{2\sigma^2}}. \tag{2}$$

This method integrates the core ideas of S transform (Pinnegar and Mansinha, 2003) and W transform (Wang, 2021), which incorporate frequency and instantaneous frequency respectively to regulate the window. By introducing adaptive local frequency $f_{\mathrm{opt\_loc}}$ and frequency f dynamic adjustment of the width and shape of the window function, the window function can adaptively focus on the dominant frequency area of the signal and reduce the frequency diffusion phenomenon. Its expression is

$$h(t,f;\tau)=\frac{f_{\mathrm{opt\_loc}}(\tau)+|\Delta f(\tau)|}{\sqrt{2\pi}k}\times\mathrm{e}^{-\frac{(t-\tau)^2}{2k^2}\left[f_{\mathrm{opt\_loc}}(\tau)+\left|f_{\mathrm{opt\_loc}}(\tau)-f\right|\right]^2}, \tag{3}$$

where k is a scalar factor; $f_{\mathrm{opt\_loc}}$ is the local frequency.

Substituting the window function $h(t,f;\tau)$ into the STFT can obtain the adaptive local frequency modulation transform (ALFMT), which is expressed as:

$$\mathrm{ALFMT}(\tau,f)=\frac{f_{\mathrm{opt\_loc}}(\tau)+|\Delta f(\tau)|}{\sqrt{2\pi}\mathrm{k}}\times\int_{-\infty}^{\infty}x(t)\mathrm{e}^{-\frac{(t-\tau)^2}{2k^2}\left[f_{\mathrm{opt\_loc}}(\tau)+\left|f_{\mathrm{opt\_loc}}(\tau)-f\right|\right]^2}\mathrm{e}^{-i2\pi ft}\mathrm{d}t. \tag{4}$$

Theoretically, the inverse transform of the ALFMT is as

$$x(t)=\int_{-\infty}^{\infty}\int_{-\infty}^{\infty}\mathrm{ALFMT}(\tau,f)\mathrm{e}^{i2\pi ft}\mathrm{d}\tau\mathrm{d}f. \tag{5}$$

To verify the ALFMT method's reversibility, a multi-component test signal is first constructed. In Fig. 1, the solid blue line denotes the original signal, and the dashed red line that reconstructed via the ALFMT method. From the figure, the original and reconstructed signals show excellent consistency in waveform shape and amplitude characteristics, indicating the ALFMT method has reliable reversibility. The signal's mathematical expression is:

$$S=2\cos(2\pi(80t))+(1+0.5\cos(2t))\mathrm{e}^{-\frac{t}{10}}\cos\left(10\pi\left(8t+6t^2\right)+0.3\cos(t)\right)+(2+0.2\cos(t))\sin(10\pi(5t+0.3\cos(6t))). \tag{6}$$

3. Adaptive local frequency

Assuming that the seismic trace is a time function, the complex trace $x_c(t)$ of the seismic trace is defined as follows (Taner et al., 1979):

$$x_c(t)=x(t)+i\mathrm{H}(x(t)), \tag{7}$$

where $\mathrm{H}(x(t))$ is the Hilbert transform of the actual seismic trace $x(t)$, and the complex seismic trace can also be expressed by amplitude and instantaneous phase as

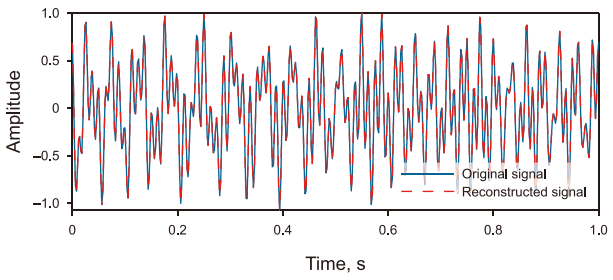

Fig. 1. Original signal (blue solid line) and reconstructed signal (red dashed line).

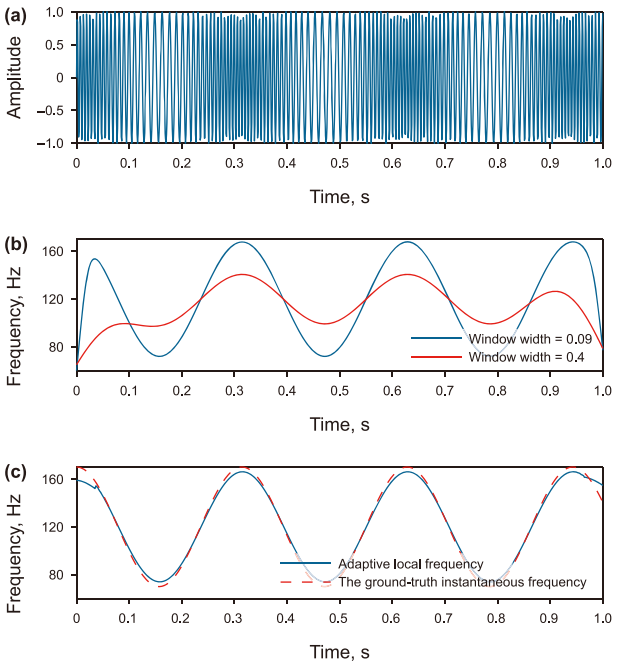

Fig. 2. Frequency characterization comparison in FM signal: **(a)** FM signal, **(b)** instantaneous frequency after the sliding window smoothing, and **(c)** adaptive local frequency and the ground-truth instantaneous frequency.

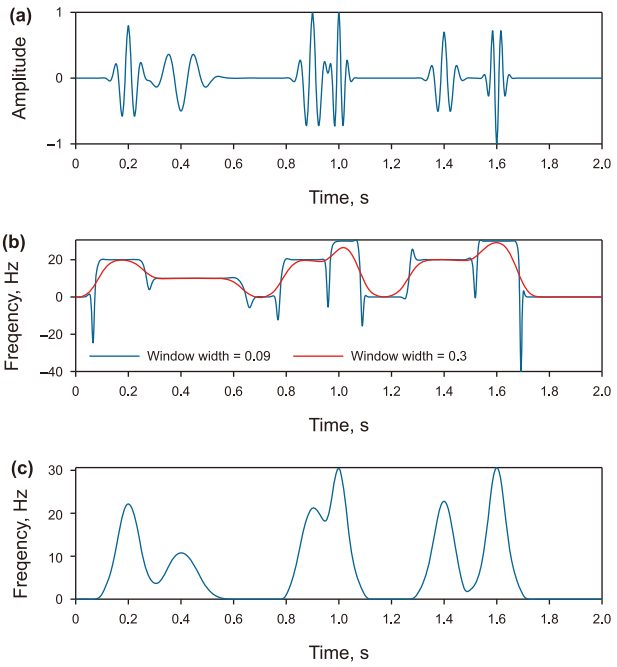

Fig. 4. Frequency characterization comparison in FM signal: **(a)** FM signal, **(b)** instantaneous frequency after the sliding window smoothing, and **(c)** adaptive local frequency.

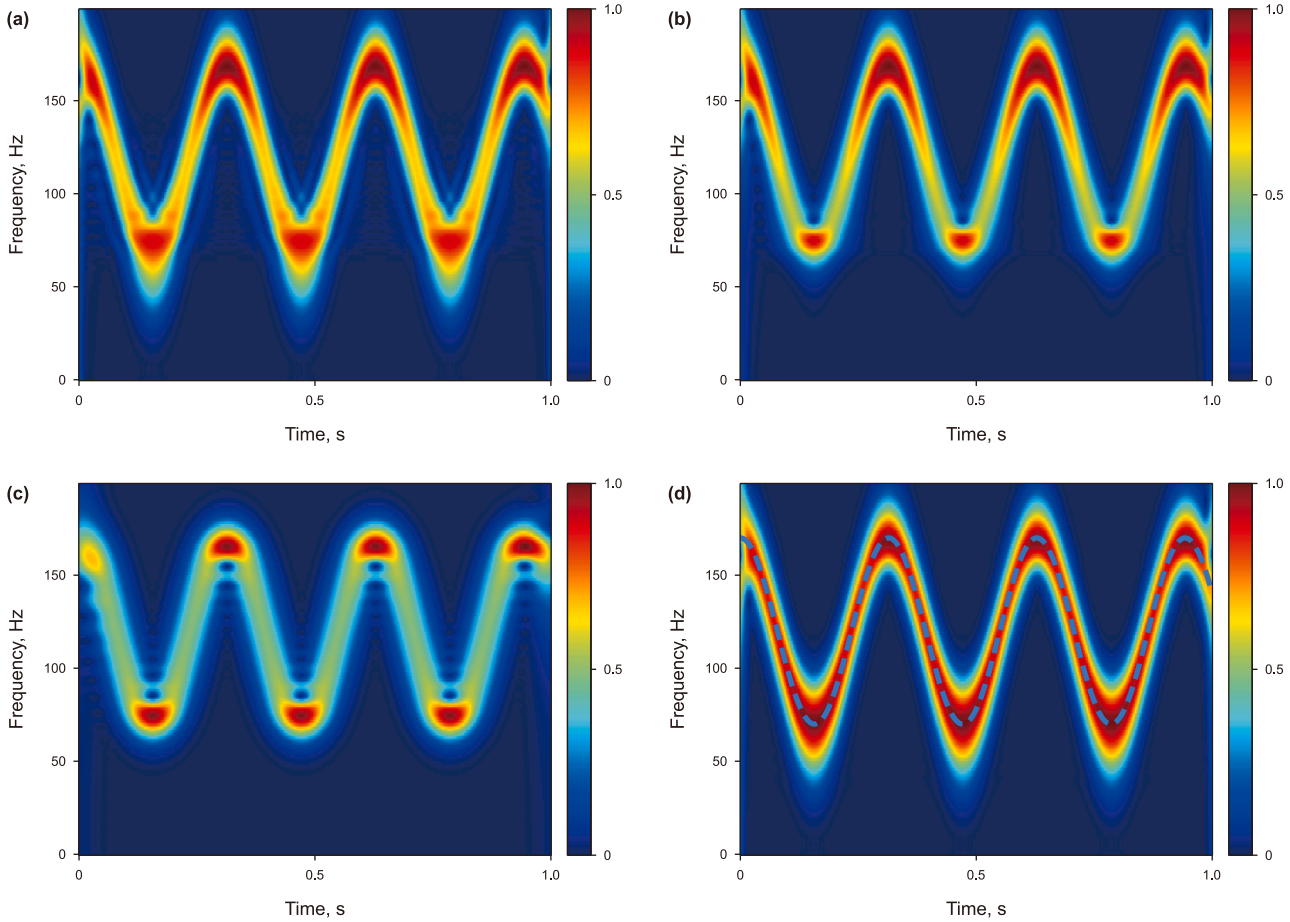

Fig. 3. Time-frequency spectrum of FM signal in Fig. 1: **(a)** WT (0.09), **(b)** WT (0.4), **(c)** STFT (0.15), and **(d)** ALFMT (blue dashed line: adaptive local frequency).

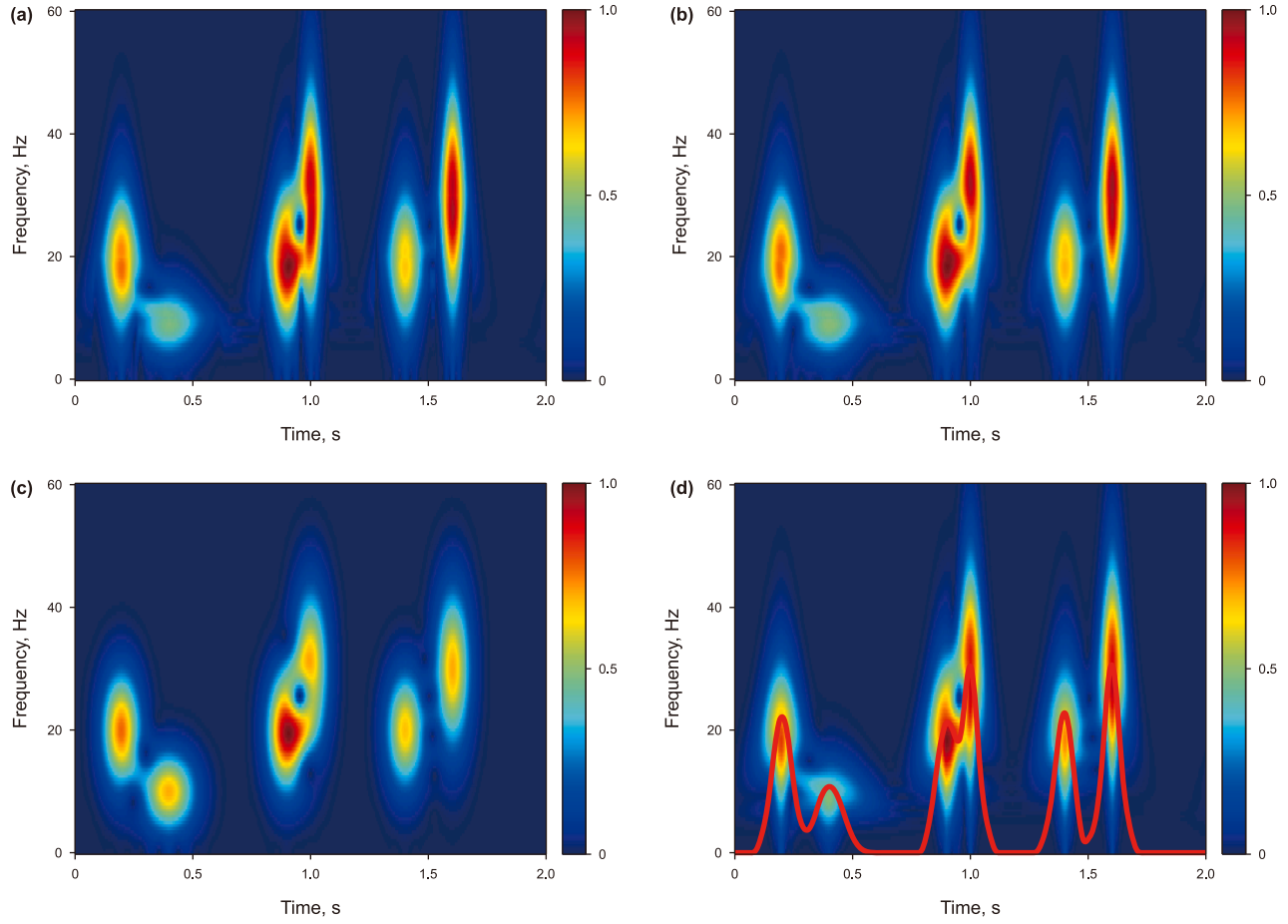

Fig. 5. Time-frequency spectrum of seismic signal in Fig. 3: **(a)** WT (0.09), **(b)** WT (0.3), **(c)** STFT (0.4), and **(d)** ALFMT (red solid line: local frequencies).

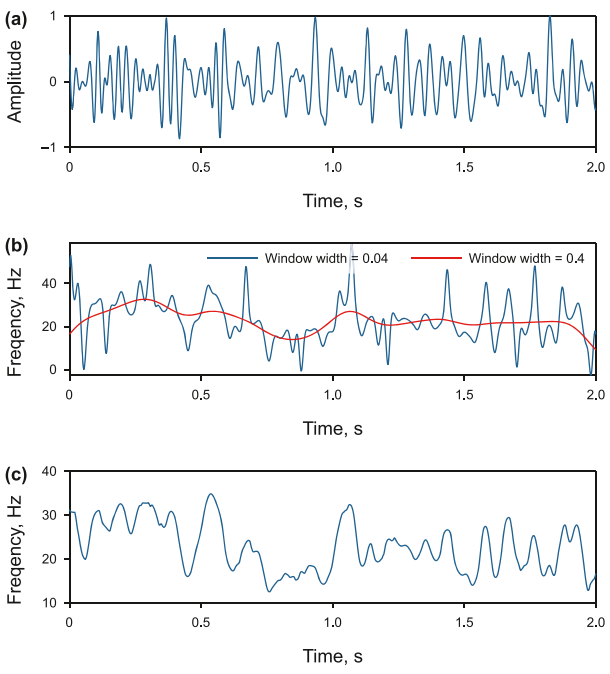

Fig. 6. Frequency characterization comparison in seismic signa: **(a)** seismic signal, **(b)** instantaneous frequency after the sliding window smoothing, and **(c)** adaptive local frequency.

$$x_c(t) = A(t)e^{i\varphi(t)}, \tag{8}$$

where $A(t) = \sqrt{x^2(t) + h^2(t)}$ is the seismic trace envelope and $\varphi(t) = \arctan(H[s(t)]/s(t))$ is the instantaneous phase

The instantaneous frequency $f(t)$ is defined as the derivative of the instantaneous phase $\varphi(t)$ (Barnes, 1992), that is:

$$f(t) = \frac{1}{2\pi}\varphi'(t) = \frac{1}{2\pi}\mathrm{Im}\left[\frac{x_c'(t)}{x_c(t)}\right] = \frac{x(t)h'(t) - x'(t)h(t)}{2\pi\left(x^2(t) + h^2(t)\right)} = \frac{n(t)}{d(t)}. \tag{9}$$

To facilitate numerical calculation, the time series is discretized into vector form. Define the diagonal matrix **D** and vectors **n** and **f**, that is:

$$\mathbf{D} = \begin{bmatrix} d_1 & 0 & 0 \\ 0 & d_2 & 0 \\ 0 & 0 & \cdots \end{bmatrix}, \ \mathbf{f} = \begin{bmatrix} f_1 \\ f_2 \\ \cdots \end{bmatrix}, \ \mathbf{n} = \begin{bmatrix} n_1 \\ n_2 \\ \cdots \end{bmatrix}. \tag{10}$$

Write Eq. (10) in matrix form as

$$\mathbf{f}_{\mathrm{inst}} = (\mathbf{D} + \varepsilon\mathbf{I})^{-1}\mathbf{n}, \tag{11}$$

where **I** is the identity matrix and ε is the damping term to avoid the division by zero problem. Although this term cannot completely stabilize the instantaneous frequency $\mathbf{f}_{\mathrm{inst}}$ estimate, it can reduce its sensitivity to noise and unstable factors (Fomel, 2007a).

The calculation of local frequency can be solved by the regularization method of linear inversion, and the shaping

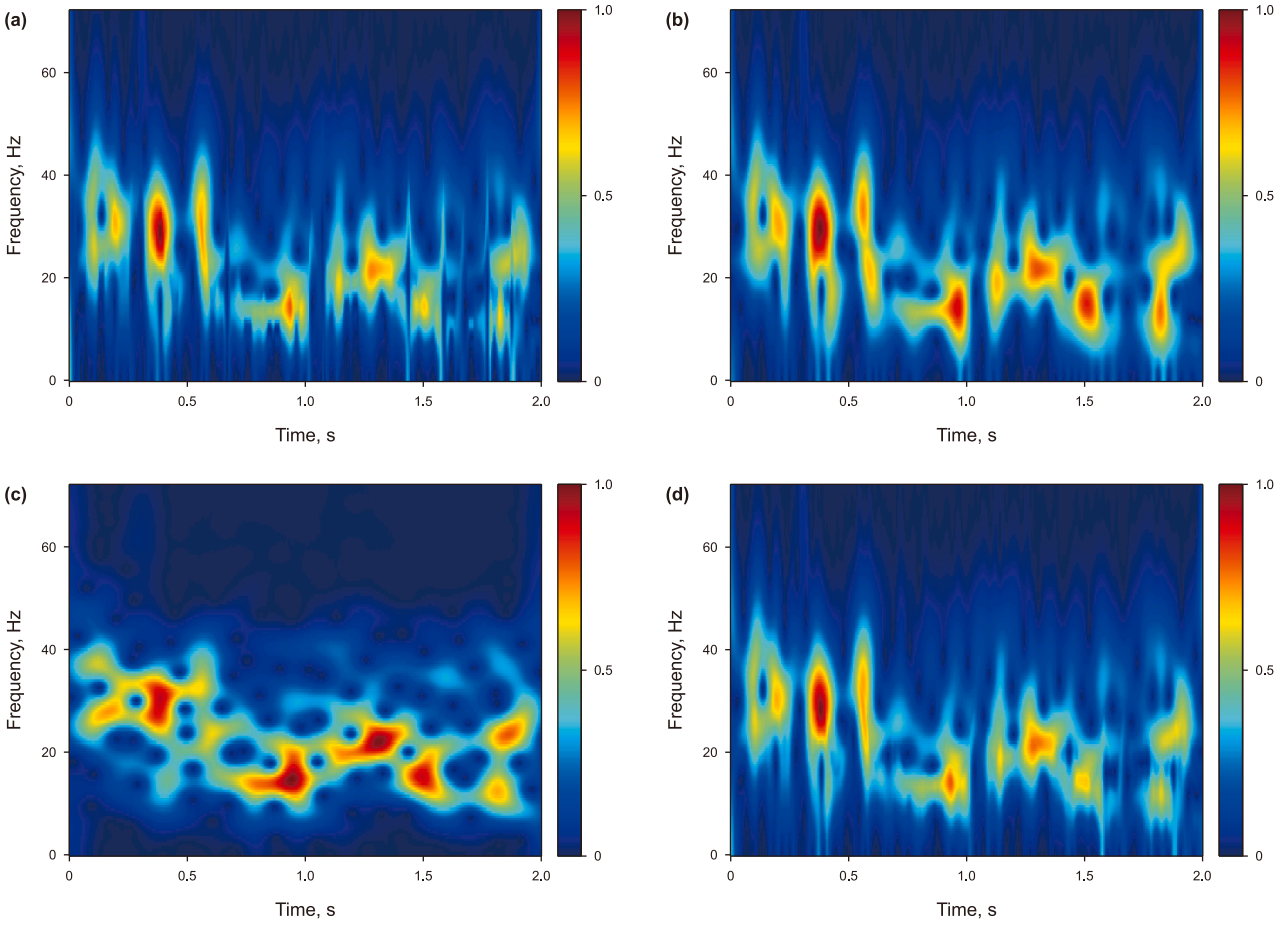

Fig. 7. Time-frequency spectrum of seismic signal in Fig. 5: **(a)** WT (0.04), **(b)** WT (0.4), **(c)** STFT (0.4), and **(d)** ALFMT.

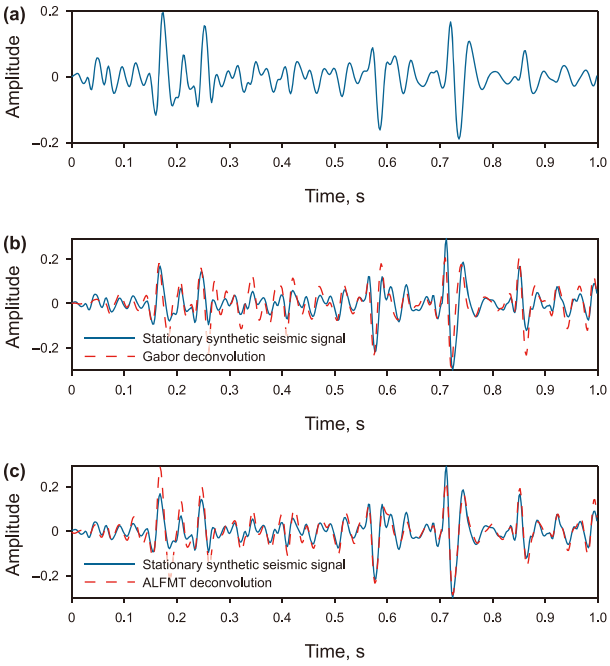

Fig. 8. Comparison of the dynamic deconvolution effect on the non-stationary synthetic seismic signal ($Q = 80$): **(a)** non-stationary signal, **(b)** stationary signal (blue solid line) and Gabor dynamic deconvolution (red dashed line), and **(c)** stationary signal (blue solid line) and ALFMT dynamic deconvolution results (red dashed line).

regularization operator S is introduced to enhance the stickiness (Fomel, 2007b), which can be expressed as follows:

$$\mathbf{S} = \left(\mathbf{I} + \xi^2 \mathbf{K}^{\mathrm{T}}\mathbf{K}\right)^{-1}, \tag{12}$$

where ξ is the smoothing factor, $\mathbf{K}$ is the first-order difference matrix, and the two jointly control the degree of smoothing of the signal. Since ξ is a constant, the smoothing scale is the same for the global data. When large or small singular values appear, increasing the smoothing scale will lead to over-smoothing of the reasonable position of local calculation. For this reason, this paper uses data energy to further construct a regularization operator as:

$$\mathbf{S}^{*} = \left(\mathbf{I} + \xi^2 \mathbf{P}^{\mathrm{T}}\mathbf{P}\right)^{-1}, \tag{13}$$

where $\mathbf{P}$ is the difference matrix based on the dynamic adjustment of local energy as:

$$P_{i,j} = \begin{cases} \sqrt{\langle A^2\rangle / \langle A^2\rangle_i}, & j = i \\ -\sqrt{\langle A^2\rangle / \langle A^2\rangle_i}, & j = i+1 \\ 0, & \text{otherwise} \end{cases}, \tag{14}$$

where $\langle A^2\rangle_i$ is the average energy in the i-th ample area, and the local frequency is as

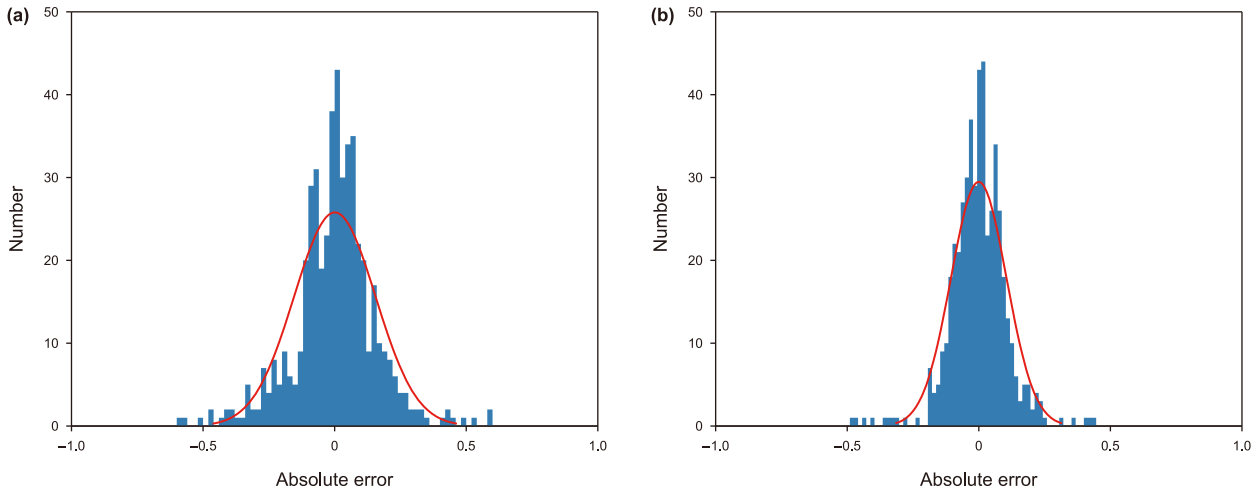

Fig. 9. Absolute error analysis of compensation results ($Q = 80$): **(a)** Gabor dynamic deconvolution, **(b)** ALFMT dynamic deconvolution.

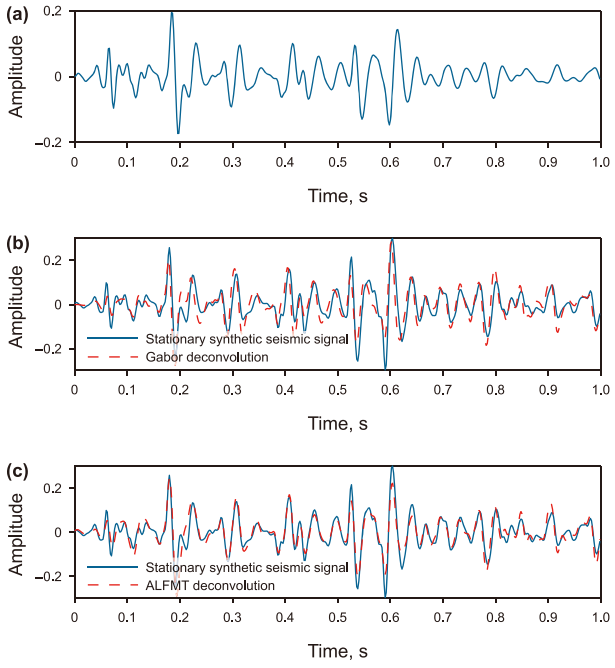

Fig. 10. Comparison of the dynamic deconvolution effect on the non-stationary synthetic seismic signal ($Q = 40$): **(a)** non-stationary signal, **(b)** stationary signal (blue solid line) and Gabor dynamic deconvolution (red dashed line), and **(c)** stationary signal (blue solid line) and ALFMT dynamic deconvolution results (red dashed line).

$$\mathbf{f}_{\text{loc}} = \left(\lambda^2\mathbf{I} + \mathbf{S}^*\left(\mathbf{D} - \lambda^2\mathbf{I}\right)\right)^{-1}\mathbf{S}^*\mathbf{n}. \tag{15}$$

In addition, to prevent over-smoothing, this paper adjusts the value of s according to the data energy in the local window, changing λ from a global constant to a local data adaptive function (Huo, 2015) as follows:

$$\lambda(t) = \sqrt{\frac{1}{N}\sum\left(x^2(t) + y^2(t)\right) + \varepsilon^2}. \tag{16}$$

Substituting the constructed λ and shaping operator $\mathbf{S}^*$ into Eq. (15), we get the final calculation formula of the adaptive local frequency as:

$$\mathbf{f}_{\text{opt\_loc}} = \left(\lambda^2\mathbf{I} + \mathbf{S}^*\left(\mathbf{D} - \lambda^2\mathbf{I}\right)\right)^{-1}\mathbf{S}^*\mathbf{n}. \tag{17}$$

4. Dynamic deconvolution based on ALFMT

Robinson (1967) proposed an important convolution model in seismic exploration, and its time domain expression is as follows:

$$\boldsymbol{s}(t) = w(t)*r(t) \equiv \int_{-\infty}^{\infty} w(\tau)r(t-\tau)\mathrm{d}\tau, \tag{18}$$

where $w(t)$ is the source wavelet and $r(t)$ is the reflection coefficient. The Robinson stationary convolution model applies to the propagation process of seismic waves without attenuation. To more accurately describe the filtering effect of underground media on the propagation process of seismic waves, Margrave proposed a nonstationary convolution model (Margrave, 1998) in which the wavelet changes with time, and the expression is as

$$s_{\text{Q}}(t) = \int_{-\infty}^{\infty}\int_{-\infty}^{\infty} a_{\text{Q}}(\tau,f)r(\tau)\mathrm{e}^{2\pi\mathrm{i}f(t-\tau)}\mathrm{d}\tau\mathrm{d}f, \tag{19}$$

where $r(t)$ is the reflection coefficient and $a_{\text{Q}}(\tau,f)$ is the attenuation function. According to the constant Q attenuation theory, the attenuation function can be expressed as

$$a_{\text{Q}}(\tau,f) = \mathrm{e}^{-\pi f\tau/Q + \mathrm{i}\mathrm{H}(\pi f\tau/Q)}. \tag{20}$$

The frequency domain expression of the non-stationary convolution model is as

$$\widehat{s}(f) = \widehat{w}(f)\int_{-\infty}^{\infty} a_{\text{Q}}(\tau,f)r(\tau)\mathrm{e}^{-2\pi\mathrm{i}f\tau}\mathrm{d}\tau. \tag{21}$$

After the inverse Fourier transform, we can get

$$\begin{aligned}\boldsymbol{s}(t) &= \int \widehat{w}(f)\left[\int_{-\infty}^{\infty} a(u,f)r(u)\mathrm{e}^{-2\pi\mathrm{i}fu}\mathrm{d}u\right]\mathrm{e}^{2\pi\mathrm{i}ft}\mathrm{d}f \\ &= \iint \widehat{w}(f)a(u,f)r(u)\mathrm{e}^{2\pi\mathrm{i}f(t-u)}\mathrm{d}f\mathrm{d}u,\end{aligned} \tag{22}$$

The expression obtained by adaptive local frequency modulation transformation of the non-steady-state signal is:

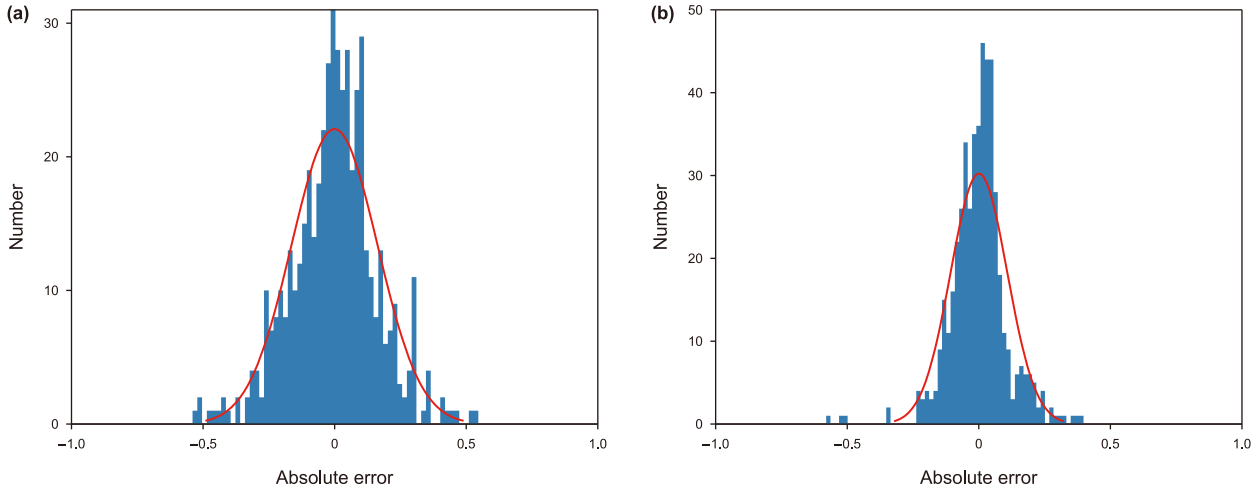

Fig. 11. Absolute error analysis of compensation results (Q = 40): **(a)** Gabor dynamic deconvolution, **(b)** ALFMT dynamic deconvolution.

$$S_{\mathrm{ALFMT}}(\tau,\nu)=\int_{-\infty}^{\infty}s(t)h(t,\nu;\tau)\mathrm{e}^{-i2\pi\nu t}\mathrm{d}t, \tag{23}$$

Substituting Eq. (22) into Eq. (23), we can obtain

$$V_{\mathrm{ALFMT}}s(\tau,\nu)=\int_{-\infty}^{\infty}\left[\iint\widehat{w}(f)a(u,f)r(u)\mathrm{e}^{2\pi if(t-u)}\mathrm{d}f\mathrm{d}u\right]h(t,\nu;\tau)\mathrm{e}^{-i2\pi\nu t}\mathrm{d}t \tag{24}$$

Integrating Eq. (24) with respect to t yields

$$V_{\mathrm{ALFMT}}s(\tau,\nu)=\iint\widehat{w}(\nu-f')\alpha(u,\nu-f')r(u)\mathrm{e}^{-2\pi i[\nu-f']u}\mathrm{e}^{-2\pi i\tau f'}\widehat{h}(f')\mathrm{d}f'\mathrm{d}u. \tag{25}$$

Let $f'=\nu-f$; then Eq. (25) is as

$$V_{\mathrm{ALFMT}}s(\tau,\nu)=\iint\widehat{w}(\nu-f')\alpha(u,\nu-f')r(u)\mathrm{e}^{-2\pi i[\nu-f']u}\mathrm{e}^{-2\pi i\tau f'}\widehat{h}(f')\mathrm{d}f'\mathrm{d}u. \tag{26}$$

Using Taylor series to expand the above formula and perform a series of simplifications, we can get

$$V_{\mathrm{ALFMT}}s(\tau,\nu)\approx\widehat{w}(\nu)\alpha(\tau,\nu)V_{\mathrm{ALFMT}}r(\tau,\nu), \tag{27}$$

where $V_{\mathrm{ALFMT}}s(t)$ and $V_{\mathrm{ALFMT}}r(\tau,\nu)$ are the adaptive local frequency modulation transformed time-frequency values of the non-stationary seismic signal $s(t)$ and the reflection coefficient $r(t)$, respectively.

Based on Eq. (27), we proposed a dynamic deconvolution algorithm based on the ALFMT. Assuming that the formation reflection coefficient sequence is a random white noise with statistical characteristics, it can be considered that the main change trend of nonstationary seismic records comes from the dynamic wavelet. Then, the minimum phase hypothesis is introduced, and the dynamic wavelet time-frequency spectrum can be expressed as

$$\widehat{w}(\nu)\alpha(\tau,\nu)\approx|V_{\mathrm{ALFMT}}s(\tau,\nu)|_{\mathrm{hs}}\mathrm{e}^{i\varphi(\tau,f)}, \tag{28}$$

where $|V_{\mathrm{ALFMT}}s(\tau,f)|_{\mathrm{hs}}$ is the smoothed nonstationary seismic record. This paper adopts the hyperbolic smoothing method proposed by Margrave et al. (2011) to process the non-stationary seismic record. The phase $\varphi(\tau,f)$ is as

$$\varphi(\tau,f)=\int_{-\infty}^{\infty}\frac{\ln|V_{\mathrm{ALFMT}}s(\tau,f')|_{\mathrm{hs}}}{f-f'}\mathrm{d}f'. \tag{29}$$

Next, the ALFMT spectrum of the reflection coefficient is estimated according to the dynamic wavelet time-frequency spectrum as

$$V_{\mathrm{ALFMT}}r(\tau,f)_{\mathrm{est}}=\frac{V_{\mathrm{ALFMT}}s(\tau,f)}{|V_{\mathrm{ALFMT}}s(\tau,f)|_{\mathrm{hs}}+\mu A_{\max}}\mathrm{e}^{-i\varphi(\tau,f)}, \tag{30}$$

where μ is a minimum value, and $A_{\max}$ is the maximum value of $|V_{\mathrm{ALFMT}}s(\tau,f)|_{\mathrm{hs}}$. This term is introduced to prevent division by zero and reduce some jitter.

Finally, the reflection coefficient time-frequency spectrum is subjected to an inverse ALFMT to obtain the formation reflection coefficient, which is then convolved with a given seismic wavelet to obtain the compensated seismic signal as follows:

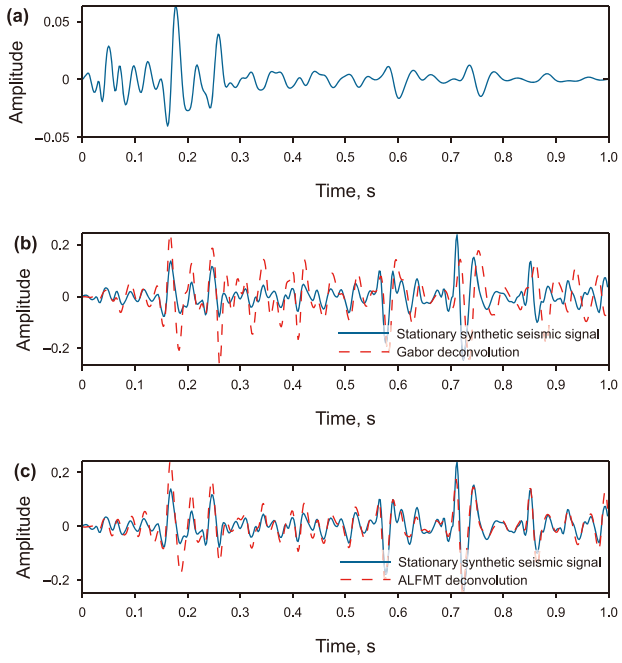

Fig. 12. Comparison of the dynamic deconvolution effect on the non-stationary synthetic seismic signal (Q = 20): **(a)** non-stationary signal, **(b)** stationary signal (blue solid line) and Gabor dynamic deconvolution (red dashed line), and **(c)** stationary signal (blue solid line) and ALFMT dynamic deconvolution results (red dashed line).

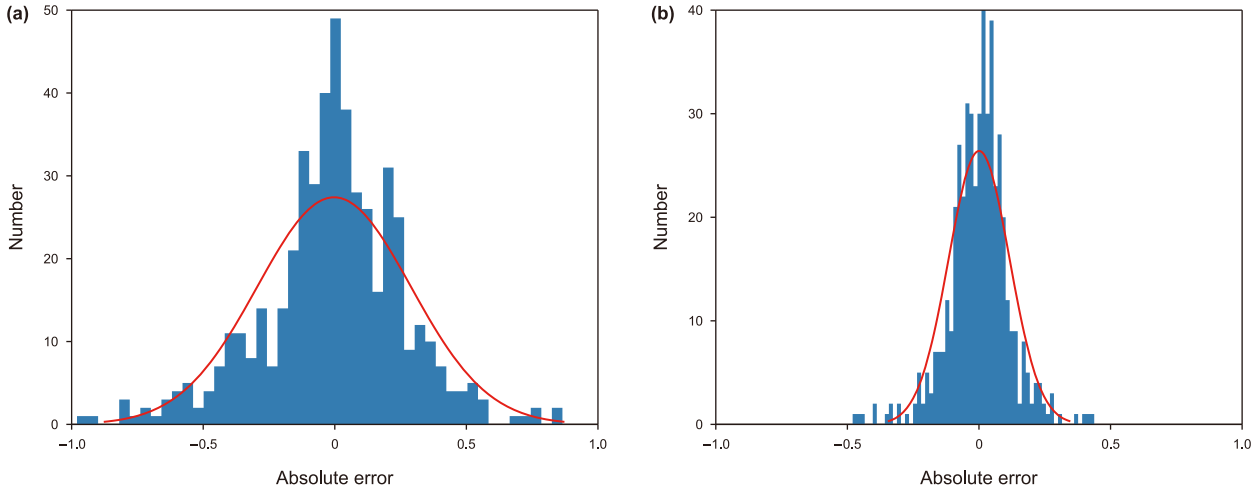

Fig. 13. Absolute error analysis of compensation results ($Q = 20$): **(a)** Gabor dynamic deconvolution, **(b)** ALFMT dynamic deconvolution.

Table 1
Pearson correlation coefficient comparison.

	Gabor dynamic deconvolution	ALFMT dynamic deconvolution
$Q = 80$	78.8%	92.4%
$Q = 40$	85.4%	90.5%
$Q = 20$	38.0%	89.8%

$$\boldsymbol{r}(t) = {V_{\mathrm{ALFMT}}}^{-1}[V_{\mathrm{ALFMT}} r(t)_{\mathrm{est}}], \tag{31}$$

$$x_{\mathrm{new}}(t) = w(t) * r(t), \tag{32}$$

where ${V_{\mathrm{ALFMT}}}^{-1}[\cdot]$ is the inverse ALFMT, $x_{\mathrm{new}}(t)$ is the compensated seismic record and $w(t)$ is the given wavelet. Herein, a Ricker wavelet with an appropriate dominant frequency is usually adopted as the wavelet; in practical application scenarios, the actual seismic wavelet can be further extracted from near-well seismic traces to improve the formation adaptability of processes such as deconvolution.

5. Numerical results

5.1. Synthetic data test of ALFMT

We first designed a nonlinear frequency modulation signal to verify the feasibility of the ALFMT. The expression of this signal is as

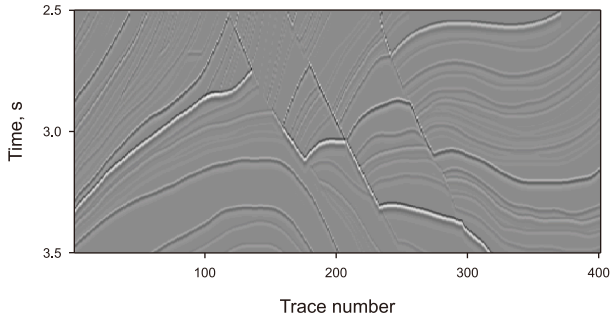

Fig. 15. Seismic profile non-attenuated Marmousi II model.

$$S = 0.6\sin(2\pi(120t + 2.5\sin(20t))). \tag{33}$$

The signal's sampling time and sampling frequency are 1 s and 1000 Hz, respectively. Fig. 2(a)–(c) shows the input signal, the instantaneous frequency smoothed using a sliding window, the adaptive local frequency obtained through the proposed method, and the ground-truth instantaneous frequency. The frequency value is relatively accurate when the window width is 0.09 s, but the phase has an apparent deviation. When the window width is 0.4 s, it cannot reflect the accurate frequency (see Fig. 2(b)). The adaptive local frequency remains unaffected by the time window,

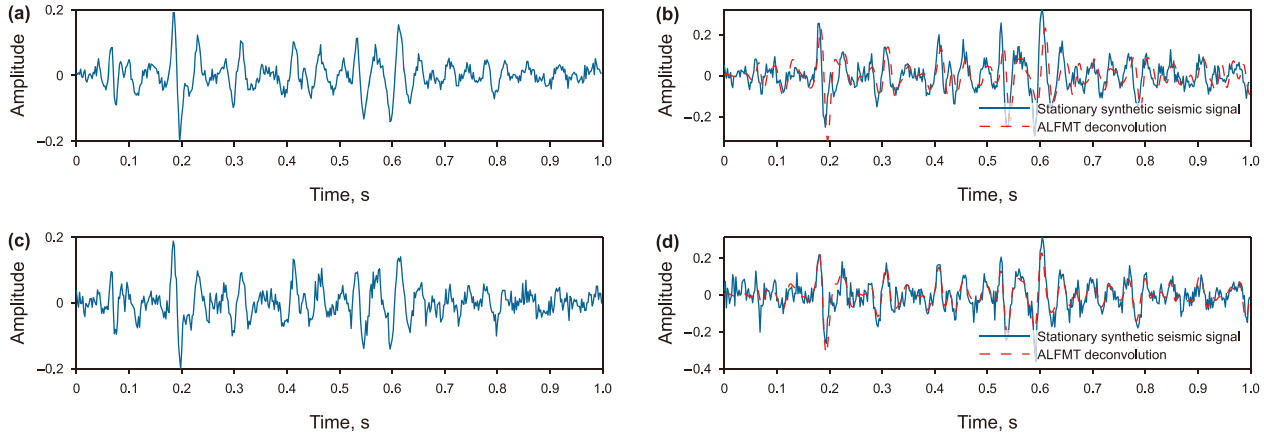

Fig. 14. Anti-noise performance test of ALFMT dynamic deconvolution on non-stationary synthetic seismic signal ($Q = 40$): **(a)** non-stationary signal (noise intensity = 0.3), **(b)** stationary signal (blue solid line) and ALFMT dynamic deconvolution (red dashed line) (noise intensity = 0.3), **(c)** non-stationary signal (noise intensity = 0.5), **(d)** stationary signal (blue solid line) and ALFMT dynamic deconvolution (red dashed line) (noise intensity = 0.5).

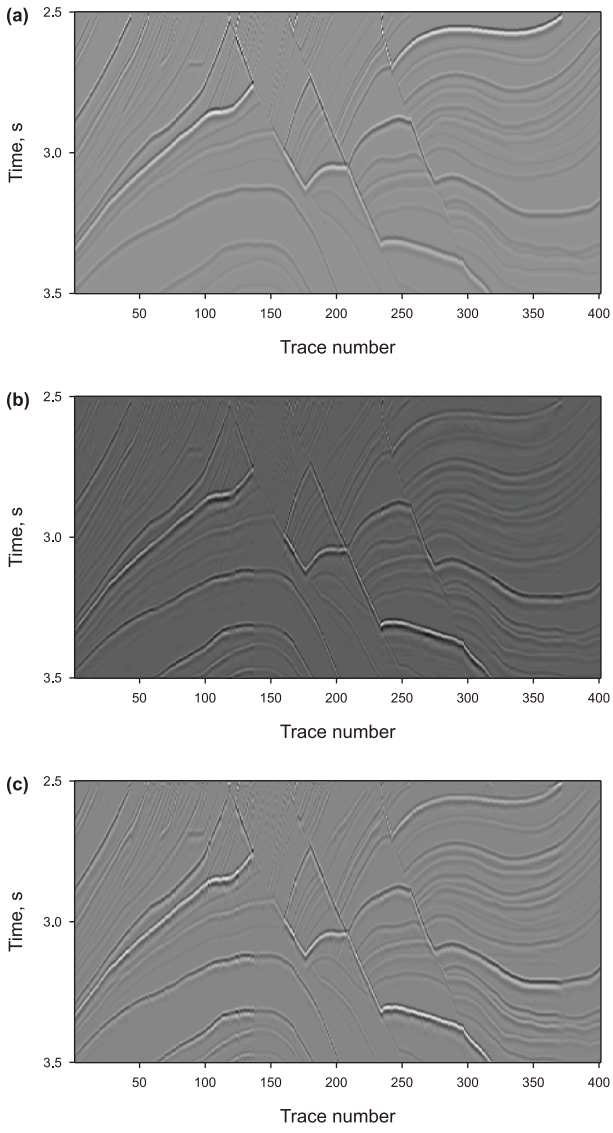

Fig. 16. Comparison of the dynamic deconvolution results for the Marmousi II model: **(a)** attenuated seismic profile ($Q = 60$), **(b)** Gabor dynamic deconvolution compensation, and **(c)** ALFMT dynamic deconvolution compensation.

and it can basically conform to the ground-truth instantaneous frequency (see Fig. 2(c)).

Fig. 3(a) and (b) shows that the time-frequency spectrum obtained by the W transform is not concentrated enough due to the influence of instantaneous frequency. The time-frequency spectrum obtained by short-time Fourier transform also has poor energy concentration (see Fig. 3(c)). However, through adaptive local frequency modulation, the time-frequency spectrum obtained by ALFMT exhibits enhanced energy concentration and more accurate frequency localization. The blue dashed line represents the adaptive local frequency, and the time-frequency distribution obtained by the method we proposed can match it well (see Fig. 3(d)).

In addition, a synthetic seismic record consisting of six Ricker wavelets was generated, with dominant frequencies of 20, 10, 20, 30, 20, and 30 Hz. The signal was sampled at 1000 Hz over a 2 s duration. Fig. 4(a)–(c) illustrates the input signal, the instantaneous frequency smoothed using a sliding window, and the adaptive local frequency obtained through the proposed method. When the window width is 0.09 s, there are significant outliers in the instantaneous frequency; however, at a window width of 0.3 s, excessive smoothing fails to accurately reflect the frequency (see Fig. 4(b)). The estimated adaptive local frequency accurately captures the time-varying frequency content of the signal (see Fig. 4(c)).

Table 2
Structural similarity Index (SSIM) comparison.

	Gabor dynamic deconvolution	ALF-WT dynamic deconvolution
$Q = 60$	82.5%	88.5%
$Q = 45$	80.4%	86.5%
$Q = 30$	73.8%	82.3%
Variable-Q	81.5%	86.2%

As shown in Fig. 5(a), (b), and (d), the ALFMT produces a time-frequency spectrum with more concentrated energy and significantly improved time resolution, enabled by adaptive local frequency modulation, compared to the WT. The red solid line in Fig. 5(d), which represents the adaptive local frequency, also confirms this point. However, the time-frequency spectrum of the STFT (see Fig. 5(c)) exhibits limited energy concentration, leading to poor time resolution.

Finally, the proposed ALFMT was applied to real single-channel seismic data acquired from a field area, with a sampling rate of 500 Hz and a recording duration of 2.4 s (see Fig. 6(a)). A window width of 0.04 s provides high time resolution and captures the local variations in instantaneous frequency but introduces singularities due to insufficient smoothing. In contrast, a window width of 0.4 s results in excessive smoothing, which fails to accurately resolve the instantaneous frequency (see Fig. 6(b)). The adaptive local frequency method effectively captures local frequency characteristics and is free from fixed window-size constraints (see Fig. 6(c)).

The WT-based time-frequency spectra shown in Fig. 7(a) and (b) are highly sensitive to variations in instantaneous frequency, resulting in reduced energy concentration. When a small window width is used, the resulting time-frequency spectrum exhibits singularities due to those present in the instantaneous frequency. In contrast, a large window width leads to insufficient temporal resolution. As shown in Fig. 7(d), the ALFMT achieves enhanced energy concentration in the time-frequency spectrum, particularly in the low-frequency range. It provides significantly better time resolution than the WT, owing to the guidance of adaptive instantaneous frequency. The time-frequency representation produced by the STFT (see Fig. 7(c)) exhibits poor energy concentration, leading to reduced time resolution.

5.2. Synthetic data test of dynamic deconvolution based on ALFMT

To verify the correctness and feasibility of dynamic deconvolution based on ALFMT, we synthesized a single-channel seismic signal using convolution theory and conducted corresponding processing and effect analysis. The synthetic seismic signal has a sampling frequency of 500 Hz and a record length of 1 s. A minimum-phase wavelet with a dominant frequency of 30 Hz is

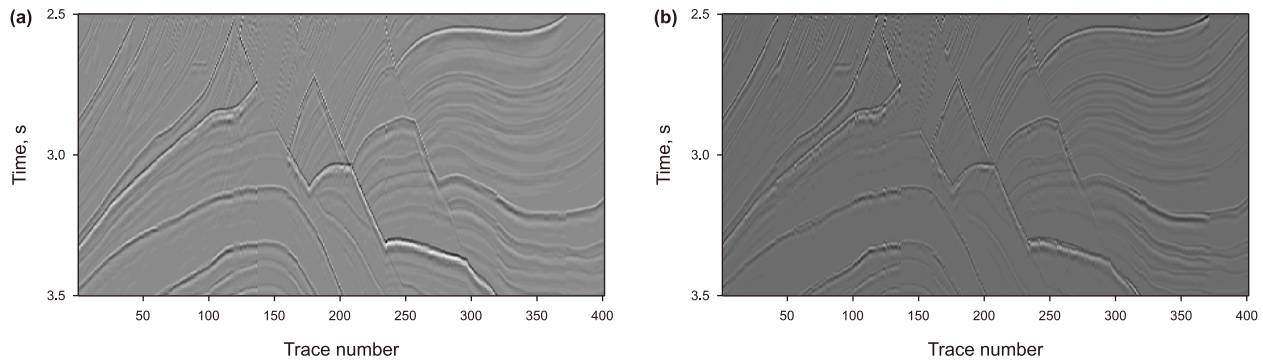

Fig. 17. Residual comparison between attenuation-compensated and original profiles ($Q = 60$): **(a)** Gabor dynamic deconvolution residual profile, **(b)** ALFMT dynamic deconvolution residual profile.

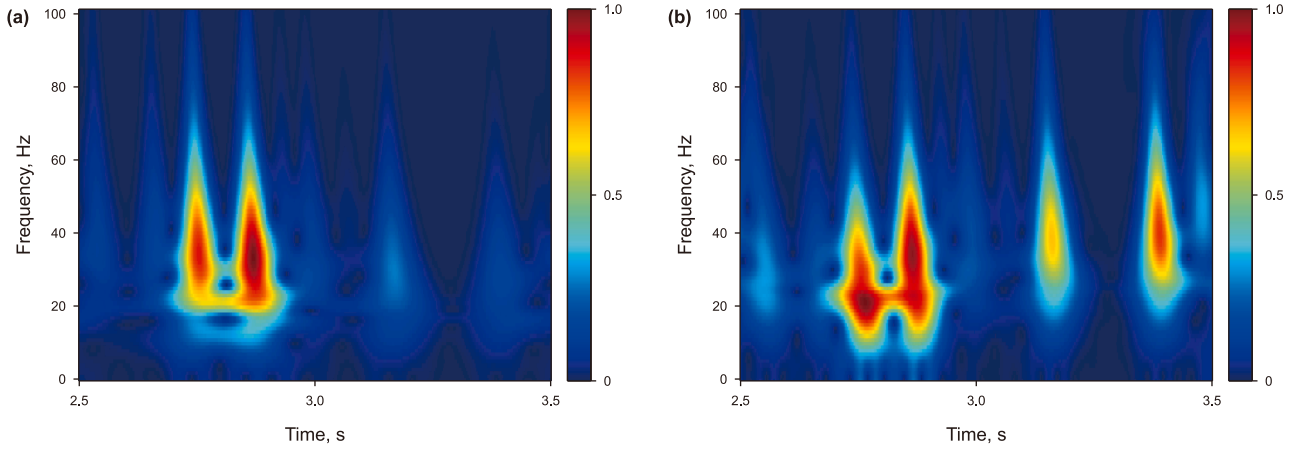

Fig. 18. Comparison of **(a)** original time-frequency spectrum of the trace 102 seismic signal with $Q = 60$ and **(b)** compensated spectrum generated by ALFMT dynamic deconvolution.

used, and the reflectivity series is modeled as Gaussian white noise. We select the quality factor parameter Q as 80 when synthesizing non-stationary seismic signals (see Fig. 8(a)). Gabor dynamic deconvolution and ALMT dynamic deconvolution are used to compensate for the non-stationary synthetic records (see Fig. 8(b) and (c)). A comparison of the results indicates that the ALFMT-based deconvolution compensation yields better phase and amplitude alignment than the Gabor-based approach. The absolute error between the non-attenuated and compensated data is computed (see Fig. 9). The error distribution shows that our proposed method achieves errors within ± 0.5, outperforming the Gabor dynamic deconvolution.

The quality factor is further adjusted to 40, and these two methods compensate for it. A comparison of Fig. 10(b) and (c) indicates that the Gabor-based compensation exhibits inferior performance. At the same time, our method can still accurately match the stationary seismic signal. The absolute error distribution at this stage indicates that the proposed method produces notably lower errors than the Gabor dynamic deconvolution (see Fig. 11).

The quality factor is adjusted to 20, and the two dynamic deconvolutions compensate for the non-stationary seismic signal. A comparison of Fig. 12(b) and (c) shows that although Gabor dynamic deconvolution compensates for the amplitude, the phase is poorly recovered, resulting in larger compensation errors. The ALFMT dynamic deconvolution results can still match the stationary seismic signals well in phase and amplitude. Even under low Q conditions, the proposed method effectively compensates for nonstationary seismic signals, maintaining the error within ± 0.5. In comparison, the Gabor dynamic deconvolution exhibits significantly higher errors (see Fig. 13).

Subsequently, by calculating the Pearson correlation coefficient between the compensated signal and the stationary synthetic seismic record, the effectiveness of the ALFMT dynamic deconvolution method in attenuation compensation is further verified. By comparing the data in Table 1 reveals that the proposed method yields more significant compensation effects at lower Q values, thereby demonstrating greater superiority.

Finally, to further verify the anti-noise performance of the proposed method, 30% and 50% noise were added to the non-stationary signal, respectively, under the condition of quality factor $Q = 40$. As can be observed from Fig. 14, the ALFMT dynamic deconvolution can still effectively compensate for the signal.

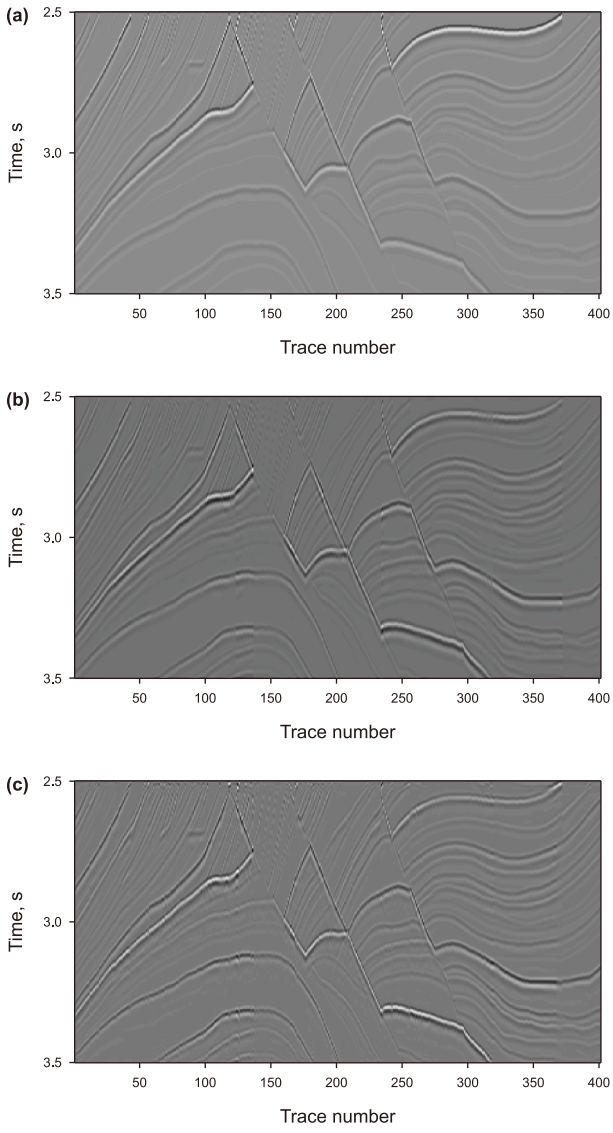

Fig. 19. Comparison of the dynamic deconvolution results for the Marmousi II model: **(a)** attenuated seismic profile ($Q = 45$), **(b)** Gabor dynamic deconvolution compensation, and **(c)** ALFMT dynamic deconvolution compensation.

5.3. Marmousi model test of dynamic deconvolution based on ALFMT

To further evaluate the performance of the ALFMT-based dynamic deconvolution on attenuated signals, seismic data from the Marmousi II model were selected for analysis. The model has highly non-stationary geological characteristics and abundant reflection events. Substantial impedance changes caused by various complex geological structures, such as faults, folds, unconformities, salt domes, and lenses, mask weak reflection signals. The model contains both high-frequency sharp features and low-frequency trends, imposing stringent requirements on the spectral recovery capability of the compensation deconvolution algorithm. The data consisted of 400 channels, each with a record length of 1 s and a sampling frequency of 500 Hz. The Ricker wavelet with a central frequency of 30 Hz is selected as the initial seismic wavelet. It is synthesized with the reflection coefficient chosen model to form a non-attenuated seismic profile (see Fig. 15).

The quality factor Q is set to 60, and the attenuation seismic record is synthesized (see Fig. 16(a)). The data is compensated using Gabor dynamic deconvolution and ALFMT dynamic deconvolution (see Fig. 16(b) and (c)). Comparing the compensation results shows that ALFMT dynamic deconvolution more accurately restores subsurface reflection structure, recovers energy lost due to absorption attenuation, and preserves amplitude and energy consistency across both deep and shallow strata. The structural similarity index (SSIM) values of the unattenuated data and the compensated data are calculated (see Table 2). The proposed method achieves 88.5%, whereas the Gabor dynamic deconvolution yields only 82.5%. By comparing the residual analysis between the compensated profiles of the two methods and the original unattenuated profile, it can be clearly observed that the proposed method exhibits smaller residual amplitudes (see Fig. 17(a) and (b)). A comparison of the time-frequency spectrum of the 102nd seismic signal before and after attenuation (see Fig. 18(a) and (b)) shows that the energy lost by attenuation has been restored, and the frequency band has been appropriately widened.

The quality factor Q is adjusted to 45, and the attenuated seismic record is synthesized (see Fig. 19(a)). Comparison of the compensation results in Fig. 19(b) and (c) shows that under more severe attenuation, significant energy diffusion occurs in the Gabor dynamic deconvolution result, leading to blurred

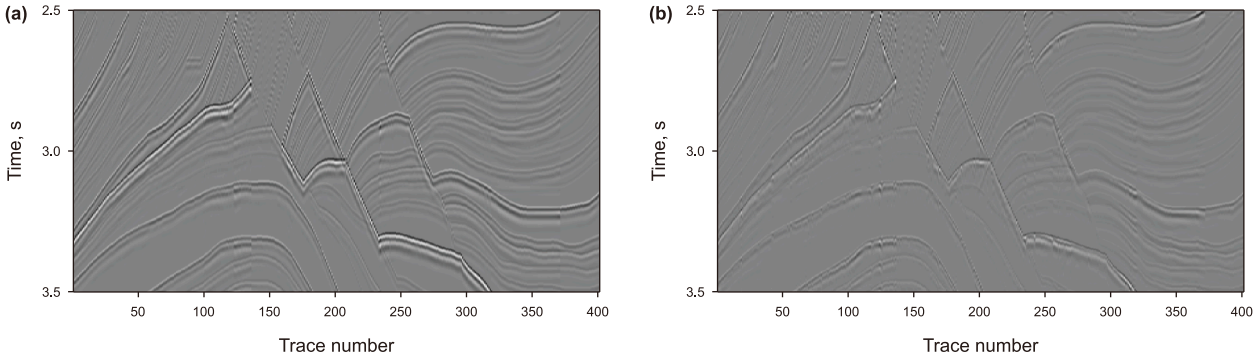

Fig. 20. Residual comparison between attenuation-compensated and original profiles ($Q = 45$): **(a)** Gabor dynamic deconvolution residual profile, **(b)** ALFMT dynamic deconvolution residual profile.

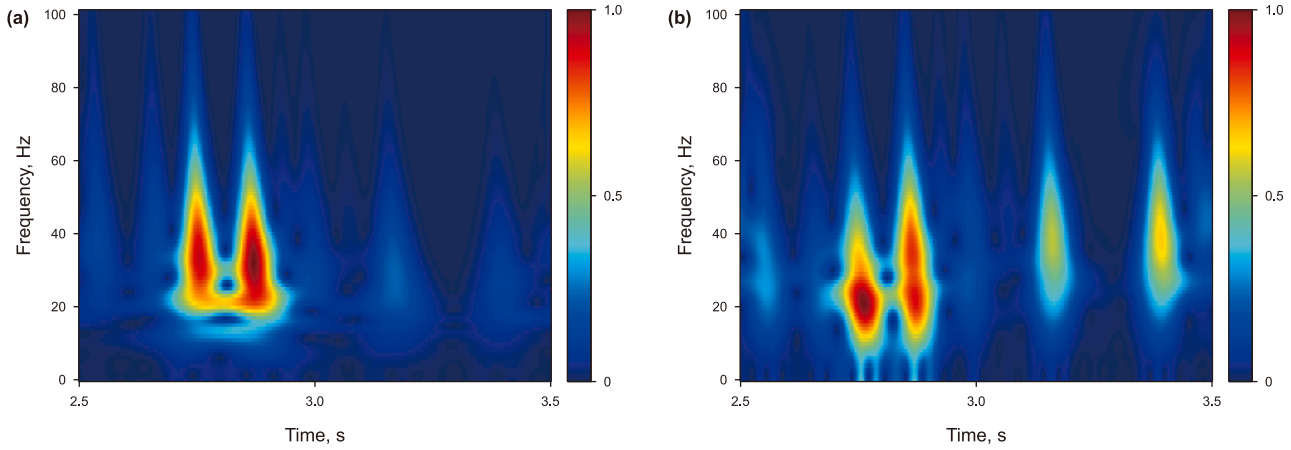

Fig. 21. Comparison of **(a)** original time-frequency spectrum of the trace 102 seismic signal with $Q = 45$ and **(b)** compensated spectrum generated by ALFMT dynamic deconvolution.

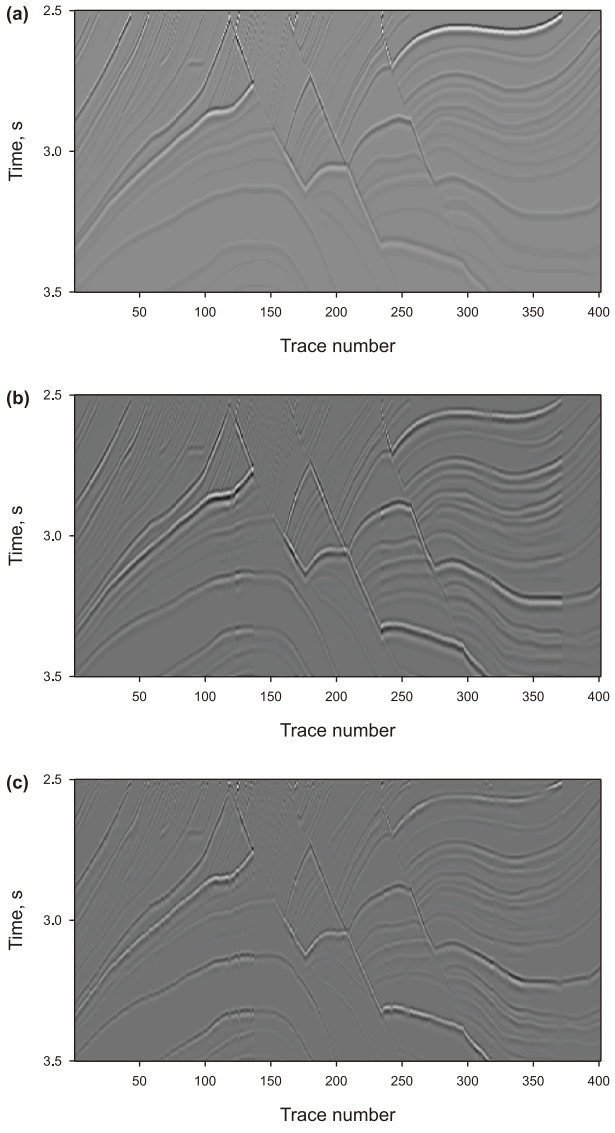

Fig. 22. Comparison of the dynamic deconvolution results for the Marmousi II model: **(a)** attenuated seismic profile ($Q = 30$), **(b)** Gabor dynamic deconvolution compensation, and **(c)** ALFMT dynamic deconvolution compensation.

boundaries between adjacent reflection layers. ALFMT dynamic deconvolution effectively restores subsurface reflection interfaces, compensates for high-frequency energy loss due to absorption, and maintains overall consistency of reflection energy and amplitude across both shallow and deep layers. The proposed method's SSIM value reaches 86.5%, while Gabor dynamic deconvolution achieves only 80.4% (see Table 2). The residual profile comparison further validates the effectiveness of our method (see Fig. 20(a) and (b)). Fig. 21(a) and (b) shows the time-frequency spectrum comparison of the 102nd seismic signal before and after attenuation. The result shows that dynamic deconvolution recovers the energy lost due to attenuation and expands the bandwidth to a certain extent.

Finally, the quality factor Q is adjusted to 30, and the attenuated seismic record is synthesized (see Fig. 22 (a)). A comparison of Fig. 22(b) and (c) shows that, even under severe attenuation, ALFMT dynamic deconvolution effectively restores subsurface reflection interfaces with an amplitude spectrum consistent with that of the non-attenuated seismic profile. However, the formation recognition of Gabor dynamic deconvolution results is reduced, and reflection overlap occurs. The SSIM values of the unattenuated data and the compensated data are calculated (see Table 2). The proposed method achieves 82.3%, while the Gabor dynamic deconvolution method achieves only 73.8%. The residual profile comparison reveals that the proposed method maintains lower residual amplitudes compared to the Gabor dynamic deconvolution results (see Fig. 23(a) and (b)). By comparing the time-frequency spectra of the 102nd seismic signal before and after attenuation (see Fig. 24(a) and (b)), it can be seen that the energy loss caused by attenuation is still effectively compensated.

Considering the spatial variability of the actual formation quality factor (Q-value), the effectiveness of the proposed method in the variable-Q model was further verified. Specific parameter settings are as follows: within the time window of 0–0.4 s, the Q-value is set to 20; 0.4–0.8 s, the Q-value is 40; and 0.8–1 s, the Q-value is 60. Two methods were respectively applied to perform compensation processing on the attenuated seismic section (see Fig. 25), and the corresponding residual sections were constructed (see Fig. 26). In addition, quantitative evaluation was conducted by calculating the SSIM between the unattenuated data and the compensated data (see Table 2). The results show that the SSIM value of the proposed ALFMT dynamic deconvolution is

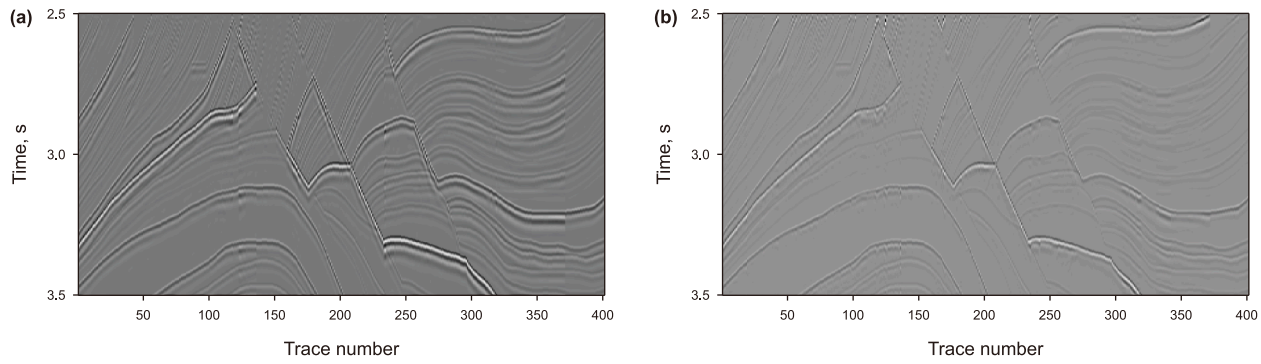

Fig. 23. Residual comparison between attenuation-compensated and original profiles ($Q = 30$): **(a)** Gabor dynamic deconvolution residual profile, **(b)** ALFMT dynamic deconvolution residual profile.

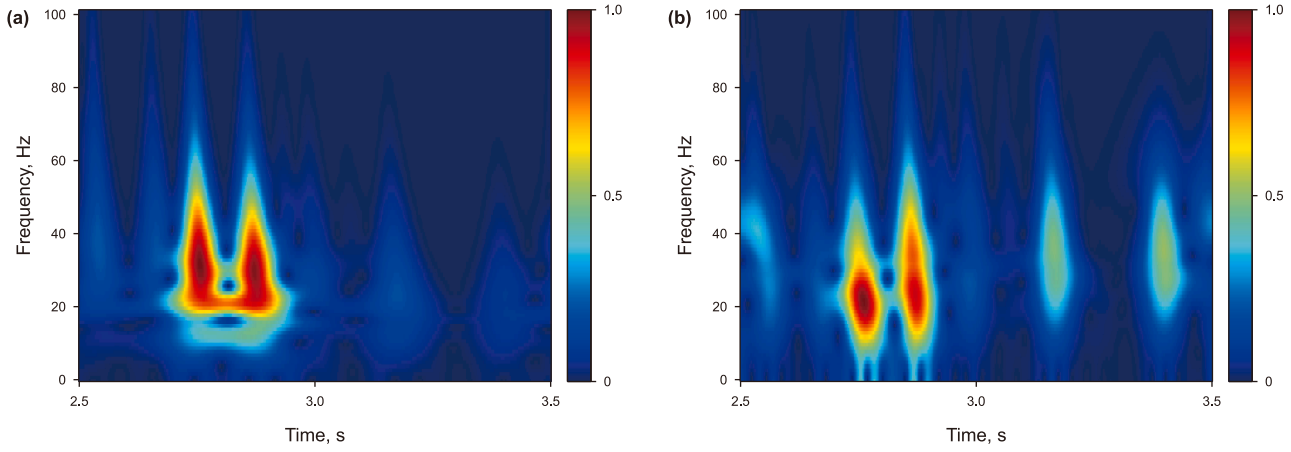

Fig. 24. Comparison of **(a)** original time-frequency spectrum of the trace 102 seismic signal with $Q = 30$ and **(b)** compensated spectrum generated by ALFMT dynamic deconvolution.

86.2%, while that of the Gabor dynamic deconvolution is 81.4%. Comprehensive analysis indicates that the ALFMT dynamic deconvolution can still achieve excellent compensation performance in the variable-Q model, which is more in line with the requirements of practical geological applications.

5.4. Actual seismic data processing of dynamic deconvolution based on ALFMT

Finally, the ALFMT deconvolution is used to process the deep seismic data of a particular work area in western China. The data contains 401 channels, each with a sampling time of 1 s and a sampling frequency of 500 Hz (see Fig. 27(a)). The region has a complex structure, with developed faults and thin interlayers. The deep energy and frequency attenuation are significant, and the phase axis energy is weakened, resulting in a disappearance of the horizon.

After applying Gabor dynamic deconvolution to the data (see Fig. 27(b)), the energy of the thin-layer event axis is enhanced. However, due to the inaccurate phase of the reflection coefficients, the resulting profile lacks structural continuity, appears disordered, and fails to preserve energy in the upper layers. From the ALFMT dynamic deconvolution results (see Fig. 27(c)), it is evident that the profile characteristics are well preserved, and high-frequency components are significantly enhanced. The thin-layer seismic reflection information becomes richer, indicating improved vertical resolution. Compared with Gabor dynamic deconvolution, the continuity of reflection events is notably improved. The stratigraphic structure is more clearly defined, and the overall seismic resolution is significantly enhanced. Seismic data compensation plays a vital role in detailed hydrocarbon prediction and the interpretation of complex subsurface structures (Zhang et al., 2022; Ji and Zong, 2023; Liu et al., 2024).

The data before and after the 101th compensation is extracted for comparison. Compared with the uncompensated seismic data shown in Fig. 28(a), both Gabor dynamic deconvolution and ALFMT dynamic deconvolution exhibit notable amplitude compensation effects, as illustrated in Fig. 28(b) and (c). Still, the result of Gabor dynamic deconvolution produces many incorrect phases, which is also why the seismic profile is messy after Gabor dynamic deconvolution compensation. Further comparison of the time-frequency spectrum before and after compensation of the trace 101 actual seismic signal reveals that the signal after ALFMT dynamic deconvolution compensation (see Fig. 29(b)) is similar to the signal before compensation (see Fig. 29(a)). The high-frequency energy information is effectively compensated, while the change in low-frequency information remains small. Combining the amplitude spectra before and after dynamic

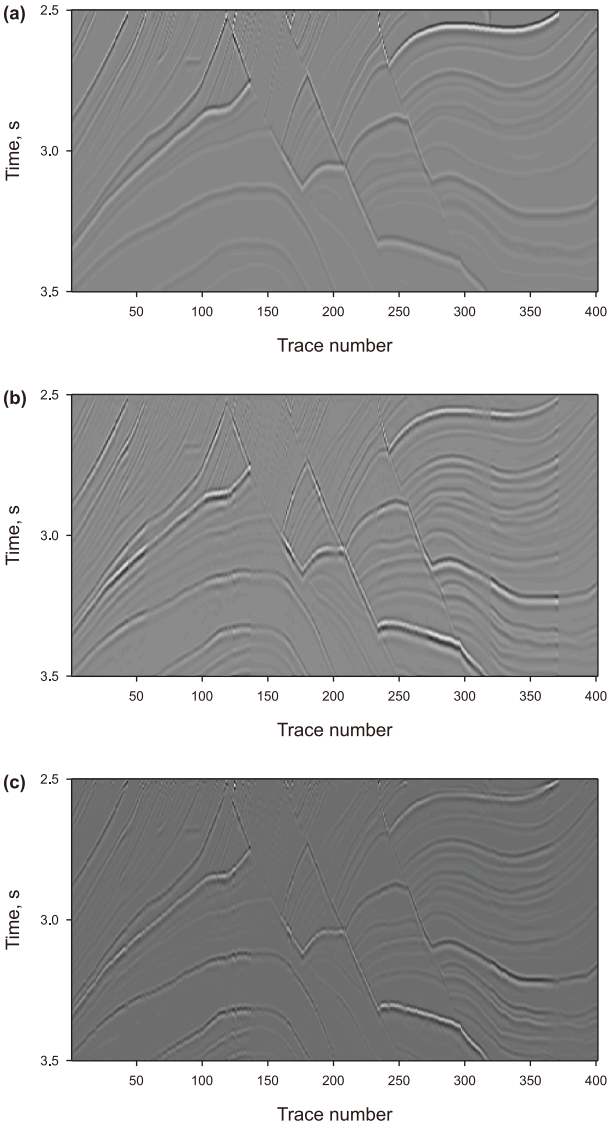

Fig. 25. Comparison of the dynamic deconvolution results for the Marmousi II model: **(a)** attenuated seismic profile (variable-*Q*), **(b)** Gabor dynamic deconvolution compensation, and **(c)** ALFMT dynamic deconvolution compensation.

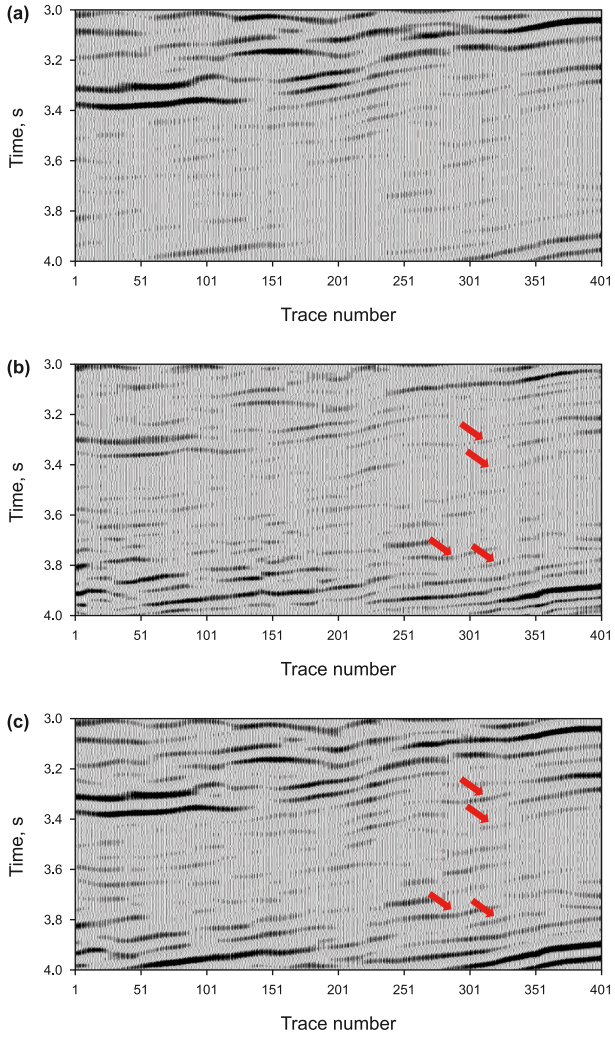

Fig. 27. Comparison of seismic profiles **(a)** without compensation, **(b)** after Gabor dynamic deconvolution, and **(c)** ALFMT dynamic deconvolution.

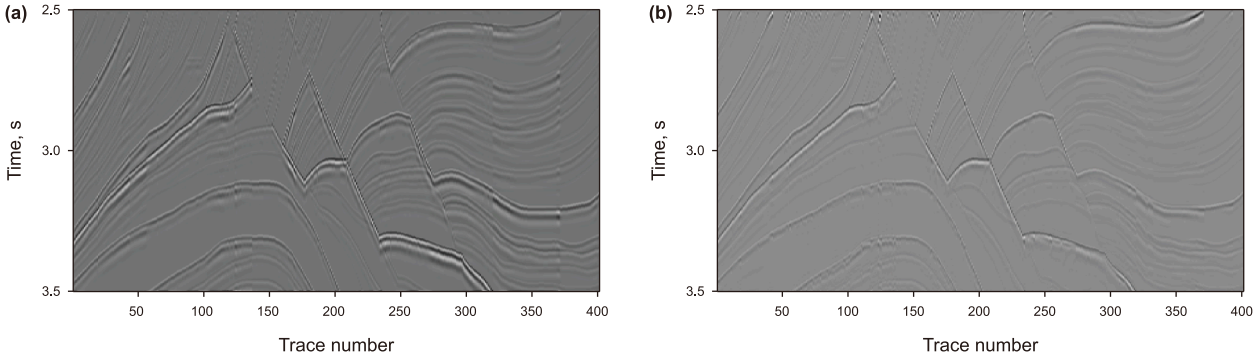

Fig. 26. Residual comparison between attenuation-compensated and original profiles (variable-*Q*): **(a)** Gabor dynamic deconvolution residual profile, **(b)** ALFMT dynamic deconvolution residual profile.

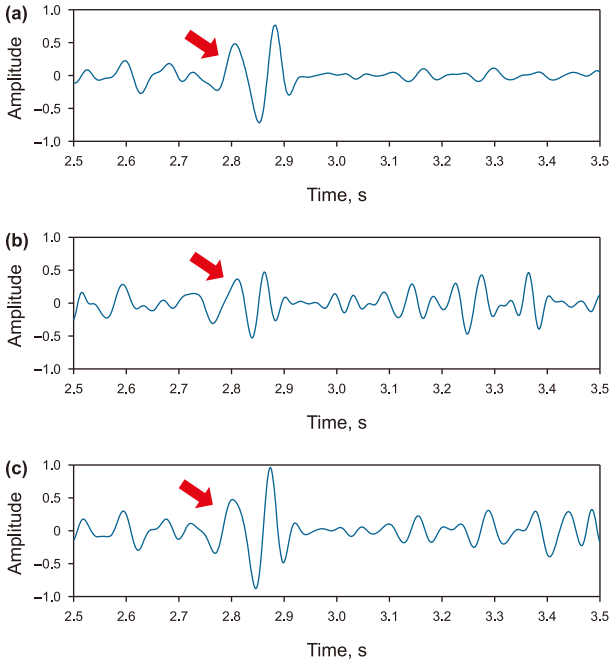

Fig. 28. Comparison of the trace 101 actual seismic signal: **(a)** without compensation, **(b)** Gabor dynamic deconvolution compensation, and **(c)** ALFMT dynamic deconvolution compensation.

deconvolution in Fig. 30, it can be observed that the frequency band range is 2–35 Hz before dynamic deconvolution. In contrast, the effective frequency band range increases to 2–40 Hz after dynamic deconvolution.

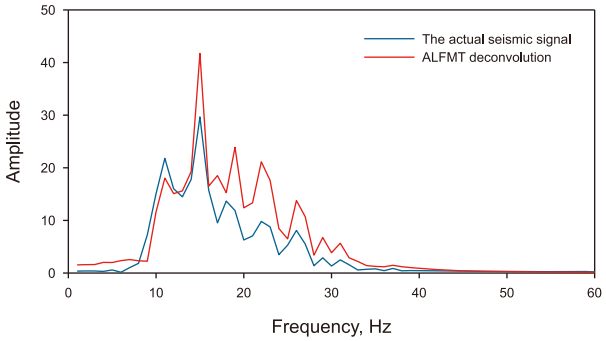

Fig. 30. Amplitude spectra comparison of the trace 101 actual seismic signal before (blue) and after (red) ALF-WT dynamic deconvolution compensation.

6. Conclusions

ALFMT is proposed by introducing adaptive local frequency to adjust the analysis window shape. Leveraging the high time-frequency resolution advantage of ALFMT, we developed an ALFMT-based dynamic deconvolution method. Modeling with sinusoidal signals, synthetic seismic data, and single-channel seismic records demonstrates that the method significantly enhances time-frequency energy concentration. The time resolution of signals at the low-frequency region is also improved. The proposed ALFMT is further integrated into a dynamic deconvolution framework. Through the high-precision time-frequency analysis method, we can more accurately convert the time-frequency domain deconvolution results into the time domain, improving the deconvolution effect and strengthening the thin-layer recognition ability. Finally, we test the new dynamic deconvolution with

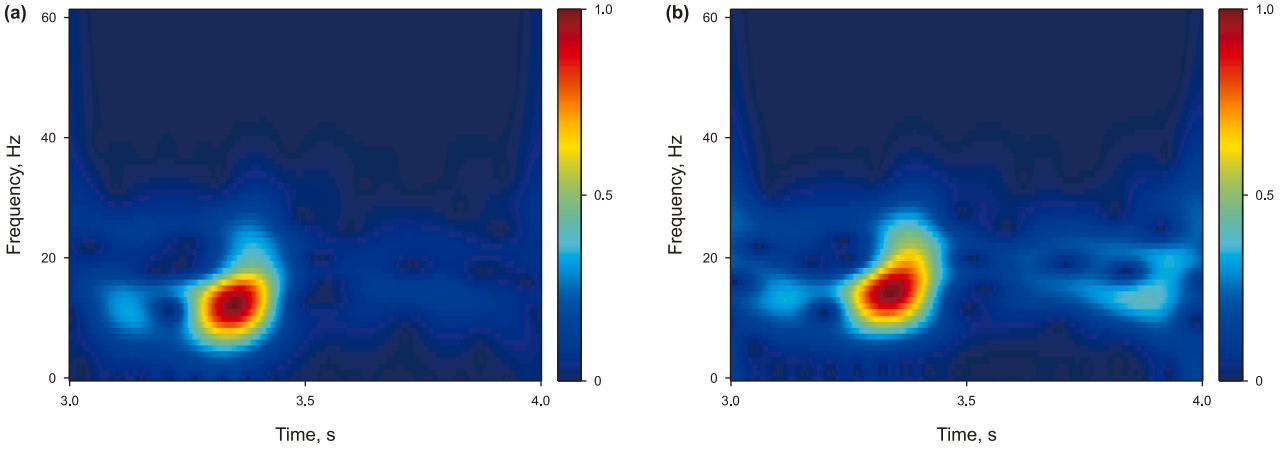

Fig. 29. Time-frequency spectrum comparison of the trace 101 actual seismic signal: **(a)** pre-compensation, **(b)** ALFMT dynamic deconvolution compensation.

the single-channel seismic record model, the Marmousi II model, and actual seismic data. The results confirm that the ALFMT-based method effectively compensates for seismic energy attenuation, thereby extending the useable seismic frequency band and enhancing seismic resolution. Although the compensated seismic data have shown significant potential in the nuanced interpretation of hydrocarbon reservoirs and complex structures, several important factors, such as the noise amplification effect caused by the attenuation of the low-frequency wavelet energy, should be considered to extend the applicability of our method.

CRediT authorship contribution statement

Mi-Mi Huang: Writing – original draft, Visualization, Software, Methodology, Investigation, Formal analysis. **Zhao-Yun Zong:** Writing – review & editing, Supervision, Resources, Funding acquisition. **Xiao-Jun Lian:** Writing – review & editing, Validation, Investigation, Formal analysis. **Yi Shen:** Writing – review & editing, Methodology, Data curation. **Ji-Dong Yang:** Writing – review & editing, Project administration, Investigation. **Qing-Feng Meng:** Writing – review & editing, Resources, Data curation.

Declaration of interests

The authors declare that they have no known competing financial interests or personal relationships that could have appeared to influence the work reported in this paper.

Acknowledgement

We cordially thank the sponsorship of the National Science and Technology Major Project of China for New Oil and Gas Exploration and Development (2024ZD1400102), the National Natural Science Foundation of China (U24B2020), the Key Technology for Geophysical Prediction of Ultra-Deep Carbonate Reservoirs (P24240) and the Fundamental Research Funds for the Central Universities (23CX10001A). Special thanks are extended to Fu-Bin Chen for his critical guidance in designing the research framework and articulating this paper.

References

Auger, F., Chassande-Mottin, É., Flandrin, P., 2012. On phase-magnitude relationships in the short-time fourier transform. IEEE Signal Process. Lett. 19 (5), 267–270. https://doi.org/10.1109/LSP.2012.2190279.

Barnes, A.E., 1992. The calculation of instantaneous frequency and instantaneous bandwidth. Geophysics 57 (11), 1520–1524. https://doi.org/10.1190/1.1443220.

Chen, C., Yang, J.D., Mu, X.R., Li, Z.C., Huang, J.P., 2023. 2D *Q*-compensated multicomponent elastic Gaussian beam migration. Pet. Sci. 20 (1), 230–240. https://doi.org/10.1016/j.petsci.2022.09.019.

Chen, F., Zong, Z., Rezaee, R., Yin, X., 2024. Pressure effects on plane wave reflection and transmission in fluid-saturated porous media. Surv. Geophys. 45 (4), 1245–1290. https://doi.org/10.1007/s10712-024-09829-9.

Chen, F., Zong, Z., Yin, X., 2022. Acoustothermoelasticity for joint effects of stress and thermal fields on wave dispersion and attenuation. J. Geophys. Res. Solid Earth 127 (4). https://doi.org/10.1029/2021JB023671 e2021JB023671.

Chen, Z., Wang, Y., Chen, X., Li, J., 2013. High-resolution seismic processing by Gabor deconvolution. J. Geophys. Eng. 10 (6). https://doi.org/10.1088/1742-2132/10/6/065002.

Cohen, L., 1989. Time-frequency distributions – A review. Proc. IEEE 77 (7), 941–981. https://doi.org/10.1109/5.30749.

Du, X., Zhuang, G., Liu, P., 2021. Comparison of two deconvolution methods. Geophys. Prospect. Pet. 60 (S1), 85–89. https://doi.org/10.3969/ji.ssn.1000-1441.2021.S1.011.

Fomel, S., 2007a. Local seismic attributes. Geophysics 72 (3), A29–A33. https://doi.org/10.1190/1.2437573.

Fomel, S., 2007b. Shaping regularization in geophysical-estimation problems. Geophysics 72 (2), R29–R36. https://doi.org/10.1190/1.2433716.

Gabor, D., 1946. Theory of communication. Part 1: the analysis of information. J. Inst. Eng. Electron. Part III Radio Commun. Eng. 93 (26), 429–441. https://doi.org/10.1049/ji-3-2.1946.0074.

Gibson, B., Larner, K., 1984. Predictive deconvolution and the zero-phase source. Geophysics 49 (4), 379–397. https://doi.org/10.1190/1.1441674.

Hargreaves, N.D., Calvert, A.J., 1991. Inverse *Q* filtering by Fourier transform. Geophysics 56 (4), 519–527. https://doi.org/10.1190/1.1443067.

Huang, N.E., Wu, Z., 2008. A review on Hilbert-Huang transform: method and its applications to geophysical studies. Rev. Geophys. 46 (2). https://doi.org/10.1029/2007RG000228.

Huo, S., 2015. Adaptive local frequency. Geophysics 80 (5), V115–V118. https://doi.org/10.1190/geo2015-0229.1.

Ji, L., Zong, Z., 2023. Lithology discrimination based on direct inversion of poisson impedance for deep tight-sandstone reservoirs. J. Geophys. Eng. 20 (1), 38–48. https://doi.org/10.1093/jge/gxac092.

Li, J., 2024. Seismic resolution enhancement based on matching pursuit algorithm. Geophys. Prospect. Pet. 63 (3), 571–577. https://doi.org/10.12431/issn.1000-1441.2024.63.03.005.

Li, R., Liu, J.B., 2018. Fast Approach for analysis windows computation of multi-window discrete Gabor transform. IEEE Access 6, 45681–45689. https://doi.org/10.1109/ACCESS.2018.2865627.

Lin, W., 2011. An adaptive generalized S-transform for instantaneous frequency estimation. Signal Process. 91 (8), 1876–1886. https://doi.org/10.1016/j.sigpro.2011.02.010.

Liu, Y., Luo, Y., Ma, Y., Liu, H., 2024. High-resolution stacking of seismic data with fast capon beamforming. IEEE Geosci. Remote Sens. Lett. 21, 1–5. https://doi.org/10.1109/LGRS.2024.3357446.

Luo, C., Zong, Z., 2023. The synchroextracting algorithm based on W transform and its application in channel characterization. IEEE Geosci. Remote Sens. Lett. 20, 1–5. https://doi.org/10.1109/LGRS.2023.3262637.

Ma, X., Huo, L.L., Li, G.F., Li, H., Meng, Q.-L., 2022. Inversion-based attenuation compensation with dip constraint. Pet. Sci. 19 (2), 543–553. https://doi.org/10.1016/j.petsci.2021.12.001.

Mallat, S.G., 1989. A theory for multiresolution signal decomposition: The wavelet representation. IEEE Trans. Pattern Anal. Mach. Intell. 11 (7), 674–693. https://doi.org/10.1109/34.192463.

Manenti, R.R., Souza, W.E., Porsani, M.J., 2018. Spectral whitening based on the singular spectral analysis method. J. Geophys. Eng. 15 (4), 1460–1469. https://doi.org/10.1088/1742-2140/aab274.

Margrave, G.F., 1998. Theory of nonstationary linear filtering in the Fourier domain with application to time-variant filtering. Geophysics 63 (1), 244–259. https://doi.org/10.1190/1.1444318.

Margrave, G.F., Lamoureux, M.P., Grossman, J.P., Iliescu, V., 2002. Gabor deconvolution of seismic data for source waveform and *Q* correction. In: the SEG Technical Program Expanded Abstracts 2002, pp. 2190–2193. https://doi.org/10.1190/1.1817142.

Margrave, G.F., Lamoureux, M.P., Henley, D.C., 2011. Gabor deconvolution: Estimating reflectivity by nonstationary deconvolution of seismic data. Geophysics 76 (3), W15–W30. https://doi.org/10.1190/1.3560167.

Naghadeh, D.H., Morley, C.K., 2017. Enhancement of temporal resolution using improved time-variant spectral whitening. J. Geophys. Eng. 14 (4), 822–832. https://doi.org/10.1088/1742-2140/aa6ddf.

Pinnegar, C.R., Mansinha, L., 2003. The S-transform with windows of arbitrary and varying shape. Geophysics 68 (1), 381–385. https://doi.org/10.1190/1.1543223.

Robinson, E.A., 1967. Predictive decomposition of time series with application to seismic exploration. Geophysics 32 (3), 418–484. https://doi.org/10.1190/1.1439873.

Taner, M.T., Koehler, F., Sheriff, R.E., 1979. Complex seismic trace analysis. Geophysics 44 (6), 1041–1063. https://doi.org/10.1190/1.1440994.

Tian, Y., Gao, J., Wang, D., 2022a. The multisynchrosqueezing optimal basic wavelet transform and applications to sedimentary cycle division. IEEE Geosci. Remote Sens. Lett. 19, 1–5. https://doi.org/10.1109/LGRS.2021.3108911.

Tian, Y., Gao, J., Wang, D., Li, Z., 2022b. Super-resolution optimal basic wavelet transform and its application in thin-bed thickness characterization. IEEE Trans. Geosci. Rem. Sens. 60, 1–12. https://doi.org/10.1109/TGRS.2022.3199450.

Tu, N., Lu, W., 2009. Inverse *Q* filtering to enhance seismic resolution. In: the 2009 IEEE International Geoscience and Remote Sensing Symposium, pp. II-345–II-348. https://doi.org/10.1109/IGARSS.2009.5418083.

Wang, B., Yin, Y., Yuan, C., Wang, P., 2021. An amplitude-and frequency-preserving S transform. IEEE Geosci. Remote Sens. Lett. 18 (7), 1154–1158. https://doi.org/10.1109/LGRS.2020.2994135.

Wang, S.Y., Chen, H., Hu, Y., Chen, X.P., 2025. Multichannel seismic resolution enhancement via spectral fitting for thin reservoir characterization. Pet. Sci. 22 (7), 2818–2827. https://doi.org/10.1016/j.petsci.2025.04.008.

Wang, Y., 2022. The high-resolution seismic deconvolution method based on joint sparse representation using logging–seismic data. Geophys. Prospect. 70 (8), 1313–1326. https://doi.org/10.1111/1365-2478.13232.

Wang, Y., 2021. The W transform. Geophysics 86 (1), V31–V39. https://doi.org/10.1190/geo2020-0316.1.

Wang, Y., 2006. Inverse *Q*-filter for seismic resolution enhancement. Geophysics 71 (3), V51–V60. https://doi.org/10.1190/1.2192912.

Wang, Y., 2004. *Q* analysis on reflection seismic data. Geophys. Res. Lett. 31 (17). https://doi.org/10.1029/2004GL020572, 2004GL020572.

Wang, Y., Rao, Y., Zhao, Z., 2024. The W transform and its improved methods for time-frequency analysis of seismic data. Petrol. Explor. Dev. 51 (4), 886–896. https://doi.org/10.1016/S1876-3804(24)60513-6.

Wang, Z., Zhang, B., Gao, J., Wang, Q., Huo, L.,Q., 2017. Wavelet transform with generalized beta wavelets for seismic time-frequency analysis. Geophysics 82 (4), O47–O56. https://doi.org/10.1190/geo2016-0342.1.

Xie, L., Wang, B., Wang, Y., Fang, J., Zeng, L., Xin, G., Shen, S., She, Z., 2024. The method for precise seismic detection of geological structures in underground coal mines and application. Front. Earth Sci. 12, 1307275. https://doi.org/10.3389/feart.2024.1307275.

Zhou, Y., Rao, Y., 2018. Seismic inverse *Q* filtering for carbonate reservoir characterization. Chin. J. Geophys. 61 (1), 284–292. https://doi.org/10.6038/cjg2018L0758.

Zhang, F., Liu, H., Zhang, L., Chen, F., Yin, X., 2016. Improved complex-trace dynamic matching pursuit algorithm. Oil Geophys. Prospect. 51 (1), 183–189. https://doi.org/10.13810/j.cnki.issn.1000-7210.2016.01.023.

Zhang, H.R., Liu, Y., Sun, Y.H., Chen, G., 2024. SeisResoDiff: Seismic resolution enhancement based on a diffusion model. Pet. Sci. 21 (5), 3166–3188. https://doi.org/10.1016/j.petsci.2024.07.002.

Zhang, Z., Yao, Z., Wang, P., 2022. Fine complex geological structure interpretation based on multiscale seismic dip constraint. Comput. Intell. Neurosci. 2022, 1–6. https://doi.org/10.1155/2022/1529935.

Zhou, H., Tian, Y., Ye, Y., 2014. Dynamic deconvolution of seismic data based on generalized S-transform. J. Appl. Geophys. 108, 1–11. https://doi.org/10.1016/j.jappgeo.2014.06.004.

Zong, Z., Fu, T., Yin, X., 2023. High-dimensional generalized orthogonal matching pursuit with singular value decomposition. IEEE Geosci. Remote Sens. Lett. 20, 1–5. https://doi.org/10.1109/LGRS.2023.3264623.